An Investigative Study on Effects of Geometry, Relative Humidity, and Temperature on Fluid Flow Rate in Porous Media

by

Nipun Thamatam

A Thesis Presented in Partial Fulfillment
of the Requirements for the Degree
Master of Science

Approved July 2019 by the
Graduate Supervisory Committee:

Jennifer Blain Christen, Chair
Michael Goryll
Trevor Thornton

ARIZONA STATE UNIVERSITY

August 2019

ABSTRACT

Developing countries suffer from various health challenges due to inaccessible medical diagnostic laboratories and lack of resources to establish new laboratories. One way to address these issues is to develop diagnostic systems that are suitable for the low-resource setting. In addition to this, applications requiring rapid analyses further motivates the development of portable, easy-to-use, and accurate Point of Care (POC) diagnostics. Lateral Flow Immunoassays (LFIAs) are among the most successful POC tests as they satisfies most of the ASSURED criteria. However, factors like reagent stability, reaction rates limit the performance and robustness of LFIAs. The fluid flow rate in LFIA significantly affect the factors mentioned above, and hence, it is desirable to maintain an optimal fluid velocity in porous media.

The main objective of this study is to build a statistical model that enables us to determine the optimal design parameters and ambient conditions for achieving a desired fluid velocity in porous media. This study mainly focuses on the effects of relative humidity and temperature on evaporation in porous media and the impact of geometry on fluid velocity in LFIAs. A set of finite element analyses were performed, and the obtained simulation results were then experimentally verified using Whatman filter paper with different geometry under varying ambient conditions. Design of experiments was conducted to estimate the significant factors affecting the fluid flow rate.

Literature suggests that liquid evaporation is one of the major factors that inhibit fluid penetration and capillary flow in lateral flow Immunoassays. The obtained results closely align with the existing literature and conclude that a desired fluid flow rate can be achieved by tuning the geometry of the porous media. The derived statistical model suggests that a dry and warm atmosphere is expected to inhibit the fluid flow rate the most and vice-versa.

ACKNOWLEDGMENTS

I would like to express my sincere gratitude towards my advisor Dr. Jennifer Blain Christen for believing in me and for providing me with the proficiency and guidance during my project. Her insightful comments and constructive criticism allowed me to explore and embrace the challenges in my research. She always made sure that I got all the backing I needed, and it had been my pleasure working with her. I would like to thank my colleagues in Dr. Christens lab, especially Mark, Sumeyra, Jon, and Ishaan, for their feedback and support during my time at Arizona State University.

I would like to thank Dr. Michael Goryll for motivating me to pursue research in biomedical applications, and I would also like to show my gratitude for agreeing to serve on my committee and for his valuable comments during the project discussion. I would like to thank Dr. Trevor Thornton for providing me with the expertise during my time at ASU and for inspiring me to pursue MEMS design and fabrication. I would also like to thank him for kindly agreeing to serve on my committee.

Most importantly, I would like to thank my parents, Shanthi and Srinivas, for their unconditional love and, concern. I would like to thank my brother Nihal, for inspiring me to pursue a career in a unique field despite the challenges. I would like to thank Bhanu, Sarath, and Shailaja for putting up with more than I ever asked for and for being there for me through thick and thin.

I am greatly indebted to you all for all you have done for me. Thank you.

TABLE OF CONTENTS

CHAPTER Page

LIST OF TABLES

LIST OF FIGURES

CHAPTER Page

Chapter 1

INTRODUCTION

The socio-economic sustainability of a country is highly dependent on its advancements in health and technology. Reliable and accurate diagnostics play an essential role in the choice of treatment and in developing public healthcare policies that are beneficial to everyone. Currently, developing countries bear 90% of the global disease burden but account for only 12% of global health expenditure (Sharma *et al.* (2015)). Over 95% of mortalities due to acute respiratory infections, malaria, HIV, and tuberculosis occur in developing countries, and Africa bears much of this disease burden (Yager *et al.* (2008)).

Mathers and Loncar (2006) estimated the global mortality rate and disease burden from 2002 to 2030. Using the data from the Global Burden of Disease project, they have projected baseline, optimistic, and pessimistic projection of various disease burden, including HIV AIDS. Global HIV/ AIDS deaths are estimated to rise from 2.8 million in 2002 to 6.5 million in 2030, and this is the baseline estimate. Figure 1.1 shows the projected life expectancy of various countries. Despite the uncertainty in predictions, the plot helps us appreciate the impacts of national health investment and health policies.

Developing countries face various health challenges, mainly due to the limited access to laboratories or medical testing facilities resulting in high mortality rates. The scarcity of water and uninterrupted power supply in rural areas are some of the reasons that amplify these issues. One way to address this is to develop easy-to-use, portable, and relatively accurate diagnostics. While the lack of access to expensive laboratories is the primary motivation for developing such systems, applications that

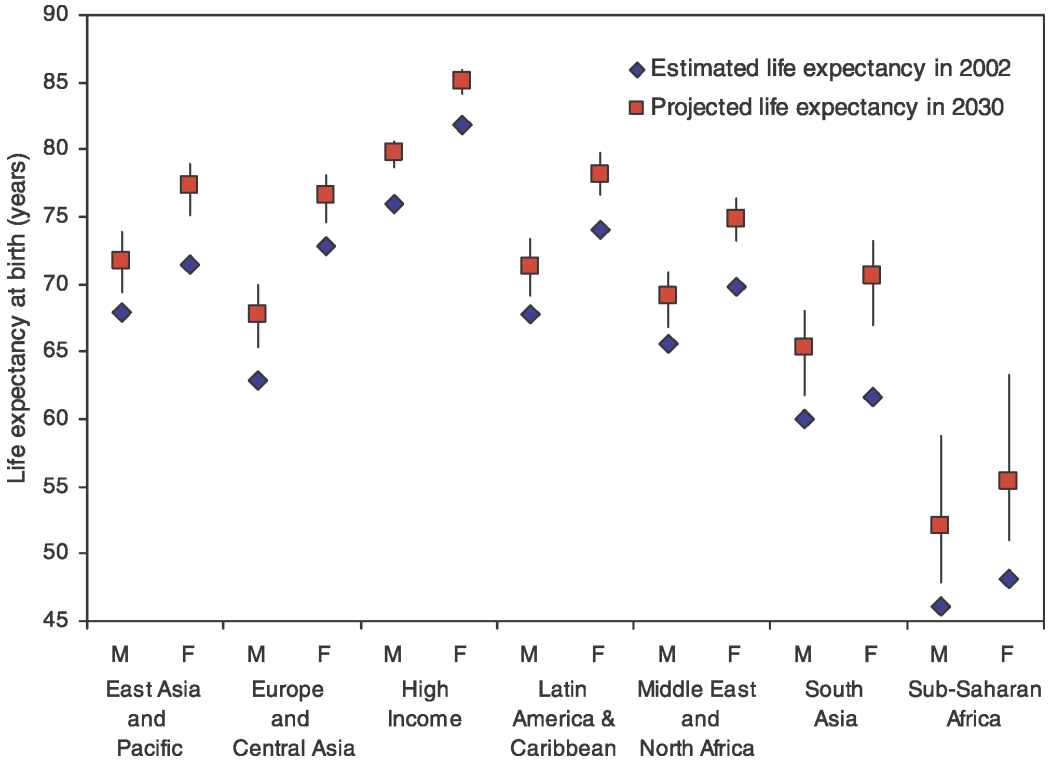

Figure 1.1: Projected life expectancy based on gender and region's income by Mathers and Loncar (2006)

require rapid analysis such as pregnancy tests demand portable point of care (POC) diagnostics as well.

1.1 Point of Care Diagnostics

An ideal point of care diagnostics test for limited-resource setting should satisfy ASSURED criteria - Affordable, Sensitive, Specific, User-friendly, Rapid and Robust, Equipment-free, and Deliverable to end-users. Figure 1.2 shows various implementations that are currently available, and they vary significantly relating to complexity.

For example, Accutest as shown in figure 1.3 is a urine test for pregnancy that satisfy most of the ASSURED criteria. The urine sample is added at the sample site denoted by 'S'. The analyte then travels to test line and control line using capillary

Figure 1.2: Commercially available Point of Care tests

Figure 1.3: An example of urine test for pregnancy manufactured by Jant Pharmacal Corporation

flow, denoted by "T" and "C" respectively. The control line indicates the validity of the test, whereas the test line suggests the presence of human chorionic gonadotropin (hCG) in urine specimens. The cassette format of the test makes it portable, and the capillary flow avoids the use of complex micro-pumps for analyte delivery. The qualitative nature of the test makes it easy to use.

One of the significant challenges of developing POC products is integration. Many

research groups are trying to develop innovative methods for fluid delivery, pre-treatment, and sample detection. However, the inclusion of these segments as an afterthought has been a significant hurdle for commercialization of POC devices. An ideally integrated POC device must offer sample collection, pre-processing, analyte reaction, sample detection, and display results to the patient. In addition to this, it should be cost-effective, portable, and easy to use. The design of these segments must be compatible with each other to achieve a highly efficient system. It has become increasingly problematic to achieve mutual compatibility with an increase in the number of components to integrate.

Chin *et al.* (2012) discuss various commercially available POC products and the challenges for commercialization. In addition to issues with mutual compatibility, they mention problems due to global health investments, business strategies, manufacturing, and regulatory approval. With respect to production, until now, most of the devices are based on glass or silicon micromachining or PDMS soft lithography. Although they offer the desired functionality, the cost of manufacturing has inhibited their commercialization. With the desire to reduce the cost of production, there is an increase in interest to develop systems based on Plastics and Paper or porous membranes. Nitrocellulose is often used in later flow assays and is very cost-effective. A system with multiple test steps can be developed by controlling, geometry, size, and porous media parameters.

In addition to the integration and cost of manufacturing, a POC device faces challenges due to the complexity of the test procedure. It includes user training, manual, and user intervention steps. Current tests that are portable and easy to use are usually qualitative or semi-quantitative and are often not sensitive or specific. Yager *et al.* (2008) discuss significant constraints in developing a quantitative diagnostic test in low resource settings. Under ideal conditions, most diagnostic tests for

infectious diseases work well, but all the platforms like microscopy and lateral flow assays perform poorly in a non-ideal resource setting. LFIAs are the most successful POC tests, but the sensitivity and specificity are not optimal for quantitative results; reagent stability under harsh conditions is one of the reasons. However, there is an increase in interest for signal amplification and quantitative LFIAs.

Specimen collection and Specimen Processing also impact the test complexity as well as test performance. The collection techniques that are available in ideal conditions are not available in low-resource settings. Therefore, the absence of ideal conditions makes it imperative to evaluate POC technologies with samples collected under harsh conditions. Sample processing includes cell isolation, plasma separation, and nucleic acid extraction. There seems to be an enormous technology gap for such sample processing techniques in a low-resource setting. In addition to these challenges, bio-waste disposal, environmental impacts, standards for evaluation are some of the issues that also require considerable attention.

With an emphasis on HIV and Tuberculosis, Schito *et al.* (2012) discuss the challenges and opportunities for low-cost point of care tests. Many Infants born in sub-Saharan Africa infected with HIV go undiagnosed due to long turnaround times and insufficient infrastructure for traditional tests such as collecting dried blood spots and performing DNA testing. Tuberculosis tests rely on central diagnostics laboratories for microscopy and chest radiography for diagnosis. POC tests with good sensitivity and specificity will significantly mitigate the challenges mentioned above by complementing the traditional techniques that require central diagnostic laboratories.

As we discussed before, there is a need to integrate biosensors and to incorporate biosensors with microfluidics gained interest as it provides many advantages for miniaturizing multi-step sophisticated tests. Some of the benefits include laminar flow, multiple sample detection, and the ability to integrate with micro-valves, micro-

pumps, and other MEMS devices. Kumar *et al.* (2013) discuss the prospective role of microfluidics in point of care diagnostics. Many academic groups are focusing on devices fabricated using materials like PDMS, glass, and nitrocellulose. Some of the microfluidics-based sensors include Enzymatic sensor, Microarrays, Opto-fluidics, Immunosensors, and Non-invasive sensors.

1.2 Lateral Flow Immunoassays

Lateral flow Immunoassays (LFIA) are among the most established point of care testing platforms applied in various areas. Human pregnancy tests in the 1970s first motivated the development of LFIA. It later extended towards diagnosing human immunodeficiency virus (HIV-1 and HIV-2), TB, and hepatitis B. The stability of LFIA, accuracy, usability with a wide range of analytes and storage were attractive features for developing countries. LFIA uses porous media that facilitates the separation, capture, and detection of the target analyte of interest. Fluid flow through porous media with small pores is majorly governed by capillary forces, thereby eliminating the need to use external pumps.

A wide variety of porous media and pore sizes are commercially available. The analyte and the application determine the porous media. Nitrocellulose membranes are the most widely used materials in LFIA applications due to the affinity for proteins, wettability, lack of interference with the assay, relatively inexpensive, and true capillarity. LFIAs meet most of the requirements of an ideal point of care tests, but the simplicity limits their performance. The pure capillarity avoids the usage of external pumps but offers limited control on the fluid flow resulting in variability in sample addition and pore precision. In addition to this, the limit of detection may result in qualitative or semi-quantitative tests. Also, it is observed that the performance of LFIAs is often affected by environmental factors such as temperature, humidity,

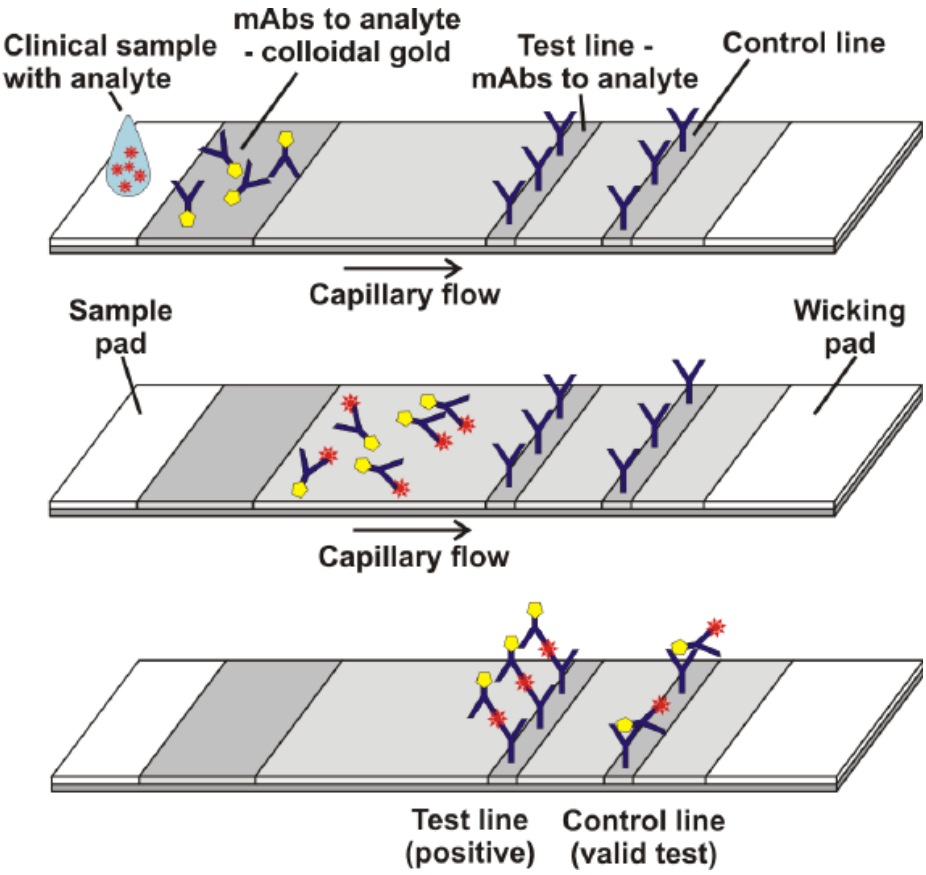

Figure 1.4: A schematic representing the working principle of Lateral Flow Immunoassays from a study by Lee *et al.* (2013)

heat, air, and sunlight.

LFIAs are highly demanded mainly due to user-friendly formats, short turnaround times, and relatively simple assay processes. Nitrocellulose, a vital component of LFIA, plays a key role by acting as a platform for reaction and as a pump to deliver fluid to the reaction site. Bahadır and Sezgintürk (2016) present a standard architecture lateral flow assay and reviews a variety of lateral flow assay implementations such as antibody-based assays, sandwich format assays, and nucleic acid-based assays.

Figure 1.4 shows a schematic representing the typical working principle of LFIAs. The target analyte from clinical sample interacts with labeled antibody, in this case,

Figure 1.5: An example of a porous structure, a pumice stone, with void space occupied by air or water

colloidal gold, already pre-loaded on the nitrocellulose membrane. The target analyte, along with antibody travels laterally through porous media using capillarity as the driving force. The migration continues until it encounters a target-specific antibody, in this case, a test line. The captured antibody-antigen-labeled antibody can be visually observed or can be measured using appropriate instrumentation. An additional control line is present to indicate the validity of the test. A wicking pad is included to avoid backflow and absorb excess reagents.

1.3 Porous Media and Nitrocellulose

Porous media is a solid matrix, that is rigid or flexible, with interconnected pores. The interconnected pores act as a bundle of channels that allows fluid flow through the solid matrix. The porous media parameters such as pore size, porosity, tortuosity, and permeability affect the fluid mass transfer rates. Common porous media include rock, soil, paper, foam, biological tissues, wood, as shown in figure 1.5. Typically, the void is filled with either single-phase (saturated) fluid like air or water or with a

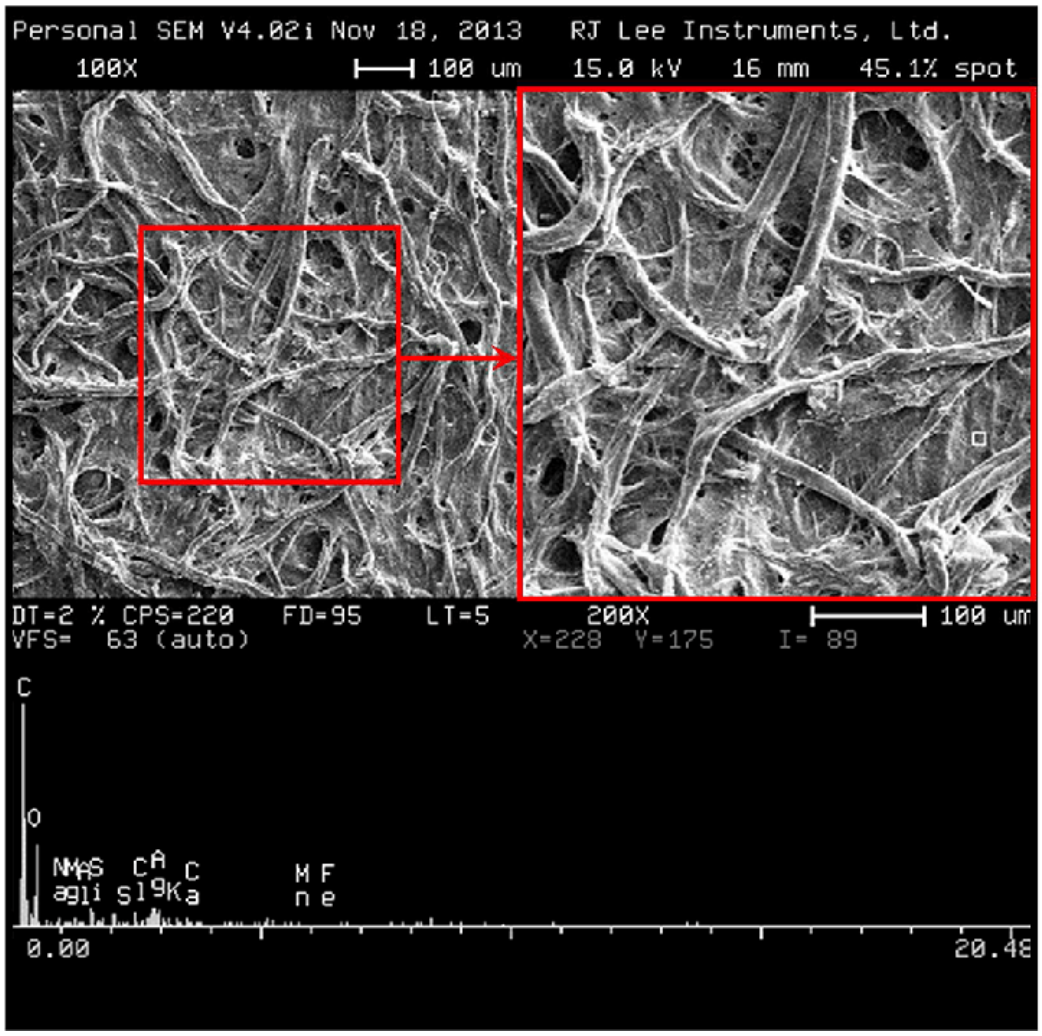

Figure 1.6: Scanning Electron Microscope image of Whatman 42 filter paper taken by Kim *et al.* (2016)

two-phase (unsaturated) fluid like water and water vapor. Some of the applications that use materials with such characteristics include filtration, petroleum engineering, bio-medical application. The usage of porous media like nitrocellulose strips in LFAs for fluid delivery and reagent reaction is justified because it is inexpensive and renders the usage of external pumps unnecessary.

Nitrocellulose or cellulose nitrate is commercially manufactured by phase inver-

sion, and the porous media parameters can be tuned by solvents used, temperature, relative humidity, and evaporation rates.Fridley *et al.* (2013) discuss the evolution of nitrocellulose material for biomedical applications. Figure 1.6 is a Scanning Electron Microscope (SEM) image of the nitrocellulose paper (Whatman Grade 42). The interaction between fluid molecules and the wall of nitrocellulose material results in capillary pressure that drives the fluid. The physics related to fluid flow in porous media and evaporation is discussed in later sections.

1.4 Motivation

Some of the factors that affect the performance of the LFIAs are reagent stability, reaction rate, and binding kinetics. A rapid reaction may affect the accuracy, and a slow reaction may affect the turnaround time. In some cases, the reduced reaction time causes insufficient time for antibody-antigen reaction and binding. In short, the fluid flow rate dictates the robustness and repeatability of LFIAs. Literature suggests that ambient conditions such as temperature, relative humidity, wind velocity can affect the fluid flow rate due to evaporation. Evaporation rate in porous media results in a viscous pressure loss, thereby inhibiting the capillary penetration and fluid velocity.

This study employs finite element (FE) analyses and experimental analyses to estimate the effects of above-mentioned parameters and the effect of geometry on fluid flow rate. First, a set of FE analyses were performed to compare various porous media modeling techniques. The accuracy of these models was compared using Newtonian and Non-Newtonian fluids. To assume a simplified case, a Newtonian fluid (water) is used for further modeling of evaporation in porous media and its dependency on relative humidity and geometry. The simulation results were validated using the design of engineering experiments.

1.5 Thesis Statement

Relative humidity and temperature affect the evaporation rate and the fluid flow rate in porous media; the geometry of the nitrocellulose membrane can be tuned to achieve a desired fluid front velocity.

Chapter 2

BACKGROUND

The objective of this study is to understand the working principles of LFIAs and to enhance the robustness of the tests by tuning fluid flow rates. This process requires a good understanding of fluid transport mechanisms in porous media. Therefore, this chapter briefly discusses the fundamental parameters and properties that determine the fluid mass transfer and energy transfer in porous media. These parameters will be invoked in later sections while formulating numerical models to address the thesis statement.

2.1 Porous Media Properties

The porosity (ϕ) of a porous media is the ratio of the volume of void space within the solid matrix to the volume of solid. Therefore, $(1 - \phi)$ is the fraction of volume occupied by solid. However, the definition of porosity assumes that all the pores are connected. In reality, a significant fraction of void space is disconnected and thereby do not contribute towards fluid flow. The actual porosity or effective porosity is defined as the fraction of connected void volume to the volume of the solid matrix. Figure 2.1 shows a schematic of porous media with interconnected and disconnected pores. The difference in porosity and effective porosity is attributed to the presence of ineffective pores.

In addition to ϕ, tortuosity (τ_p) indicates the ratio of the curved or actual length a fluid molecule has to travel to the length of the porous media. Tortuosity along with pore size (r) incorporate geometrical properties of the porous media. These properties are necessary in determining the mass transfer and energy transfer in

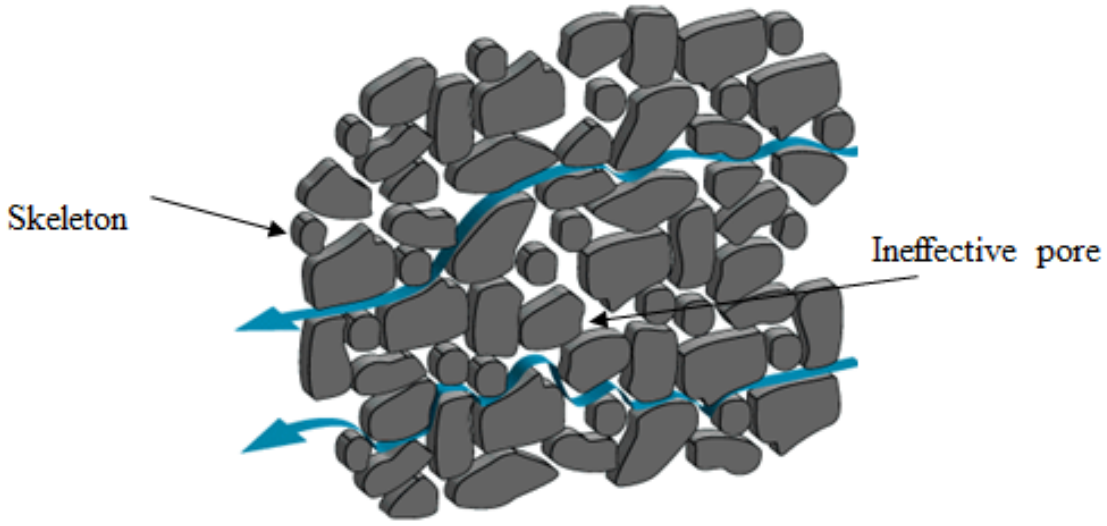

Figure 2.1: A schematic of porous media with interconnected and disconnected pores

porous media. When dealing on a macro scale, such as LFIAs, a continuum approach with permeability (k) as the lumped parameter is more practical. Permeability is determined by geometrical and fluid properties of the system.

2.2 Fluid Properties

In addition to porous media parameters, fluid parameters such as density (ρ), surface tension (σ), contact angle (θ) and dynamic viscosity (μ) determine the mass and energy transfer in porous media. Since some of the fluids in interest for biomedical applications are Non-Newtonian, it is essential to understand the effects of dynamic viscosity on fluid flow in porous media. Therefore, this section briefly discusses different types of fluids based on viscosity.

Dynamic viscosity or viscosity (μ) of fluid is the degree of resistance to deformation at a given shear rate. A Newtonian fluid is any fluid that demonstrates a linear relationship between shear stress and shear rate, as shown in equation 2.1.

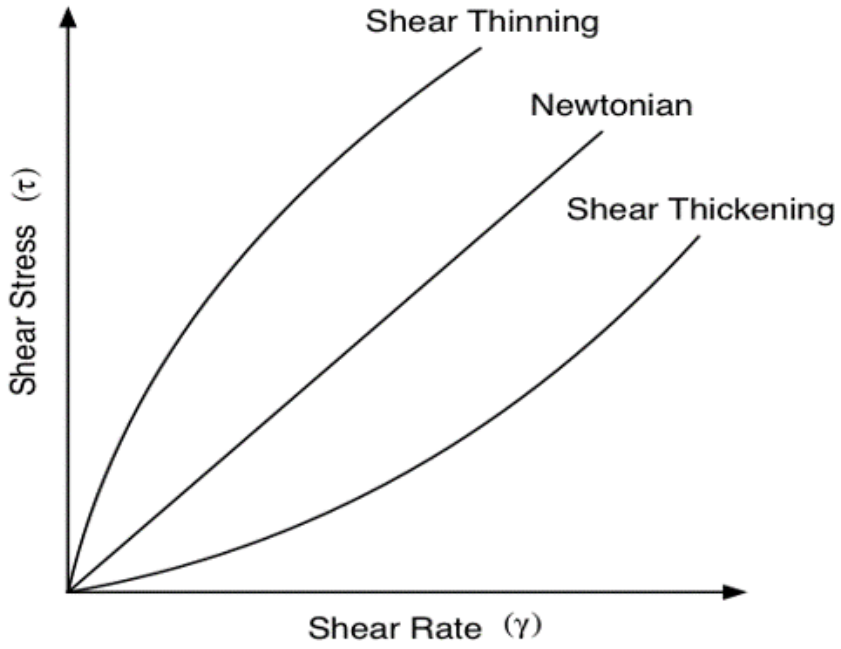

Figure 2.2: Newtonian and Non-Newtonian fluids, respectively, demonstrate the linear and non-linear relationship between shear stress and shear rate

$$\tau = \mu \frac{du}{dy} \tag{2.1}$$

where τ is the shear stress, μ is the dynamic viscosity and $\frac{du}{dy}$ is the local shear velocity (γ). The viscosity is constant in the case of Newtonian fluids. Any fluid that does not follow a linear relationship is called Non-Newtonian fluid. In this case, the viscosity can either increase or decrease under stress. Figure 2.2 plots the relation between shear stress and shear rate; the slope of the curve represents the dynamic viscosity. For a shear thickening fluid, such as starch solution, the viscosity (slope) increases as the shear rate increases. Shear-thinning fluid, such as blood or ketchup, exhibits a reduction in fluid viscosity (slope) with an increase in shear rate.

Chapter 3

LITERATURE REVIEW

The geometry of the model often determines the accuracy of the finite element (FE) analysis model. Therefore, the most accurate model is the one that closely represents the interconnected pores at micro-scale. However, discretizing a complex geometry and solving for a solution is computationally expensive, and hence, a simplified model is often desired if it results in solutions within an acceptable range. To compare the FE models for porous media, blood is used as the reference fluid as it can be modeled as both Newtonian and Non-Newtonian fluid. Later, water is used as the reference fluid to simulate the effects of evaporation on porous media due to the ease of experimental validation. The following section reviews the available literature on fluid properties, porous media properties, and techniques to model fluid flow and evaporation in porous media.

3.1 Properties of Blood

Blood is often modeled as a Newtonian fluid by neglecting the shear-thinning characteristics of it. The dynamic viscosity stays constant during the simulation and is independent of the geometry. Although this approximation is valid for higher velocities in wider channels or extremely low velocities, a Newtonian model of blood results in inaccuracies when it comes to intermediate speeds such as flow in Lateral Flow Immunoassays. The most common Non-Newtonian models of human blood are Power Law, Casson model, Walburn-Schneck model, Carreau, and Carreau Yasuda model. Since blood demonstrates non-zero viscosity at zero shear rates, Carreau Yasuda model is more appropriate for numerical analysis and will be discussed in

Table 3.1: Newtonian and Non-Newtonian properties of blood.

Parameters [units]	Newtonian Model	Carreau Yasuda Model
$a[1]$	-	0.500
$\lambda[s]$	-	0.021
μ_0 [mPa.s]	-	150.000
μ_∞ [mPa.s]	3.892	3.500
$n[1]$	-	0.342

section 4.1.

To test the influence of blood's dynamic viscosity, Mach *et al.* (2016) have modeled a bent intracranial blood vessel with flow diverting stunt. To estimate the velocity profile of the bloodstream, they measured the viscosity of human blood at different shear velocities and determined the parameters for Non-Newtonian fluid model. The estimated parameters for both Newtonian and Carreau Yasuda model are shown in table 3.1. Where a is the dimensionless factor, λ is the relaxation time, μ_0 is the viscosity at zero shear rate, μ_∞ is the viscosity at infinite shear rate and n is the power index.

3.2 Properties of Whatman Filter Paper

The porosity of a porous media fundamentally characterizes the material, and multiple experimental methods determine this parameter. The techniques include porometry, porosimetry, image analysis, and void network modeling. Gribble *et al.* (2011) present a quantitative comparison between these techniques by performing experimental analysis on seven different porous media, including nitrocellulose. It was

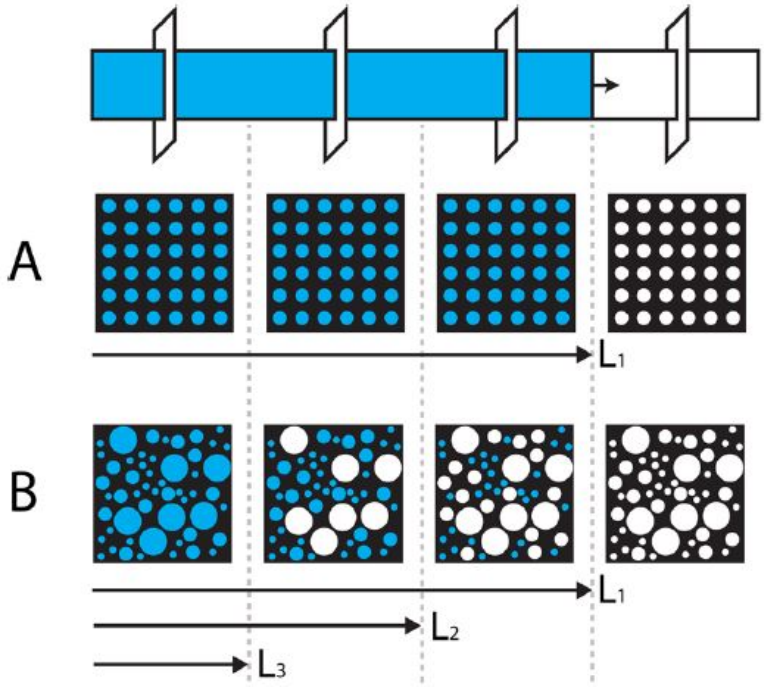

Figure 3.1: A schematic representing the Lucas-Washburn approximation of capillary flow in porous media. A) Single pore size. B) Three different pore sizes taken from Cummins *et al.* (2017)

concluded that the porometry resulted in unrealistically narrow void size distribution, and the mercury porosimetry underestimated a large number of voids. However, the error of mercury porosimetry was significantly mitigated by using a void network model. Therefore, mercury porosimetry was confirmed to be a robust method for estimating porosity.

With information on pore-sizes and porosity, various numerical models can be developed to understand fluid behavior in porous media. Figure 3.1(A) shows the schematic representation of the Lucas-Washburn approximation for capillary flow in porous media. The model approximates the porous media as a bundle of cylindrical channels with a single pore size and estimates the fluid front position as a function of time. In addition to this, the model also assumes complete saturation behind the liq-

Table 3.2: Porous media parameters for Grade 1 Whatman filter paper

Parameters [units]	Value
ϕ[1]	0.55
$r[\mu m]$	1 to 20
θ_{water} [radians]	1.309
θ_{blood} [radians]	0.908
$K_{dimensionless}$ [1]	0.0063

uid front. However, the porous media, like nitrocellulose paper, often demonstrates a distribution of pore sizes and is not fully saturated behind the liquid front. Therefore, these assumption results in inaccurate estimation for fluid flow rate.

To mitigate these inaccuracies Cummins *et al.* (2017) developed a time-dependent model for estimating the fluid flow rate in porous media with multiple pore size. Figure 3.1 part B represents the extension of the Lucas-Washburn approximation. Where L_1, L_2, L_3 are the fluid fronts of capillaries with three different pore sizes. They performed experimental analysis to estimate the pore size, contact angle, and permeability of Whatman filter paper Grade 1 to estimate the liquid front velocity. The pore sizes were determined by mercury porosimetry, and the contact angle and the dimensionless permeability were determined by vertical imbibition. The porous media parameters for Grade 1 Whatman filter paper are shown in table 3.2. The contact angle for blood and Whatman paper was obtained from Chao *et al.* (2016).

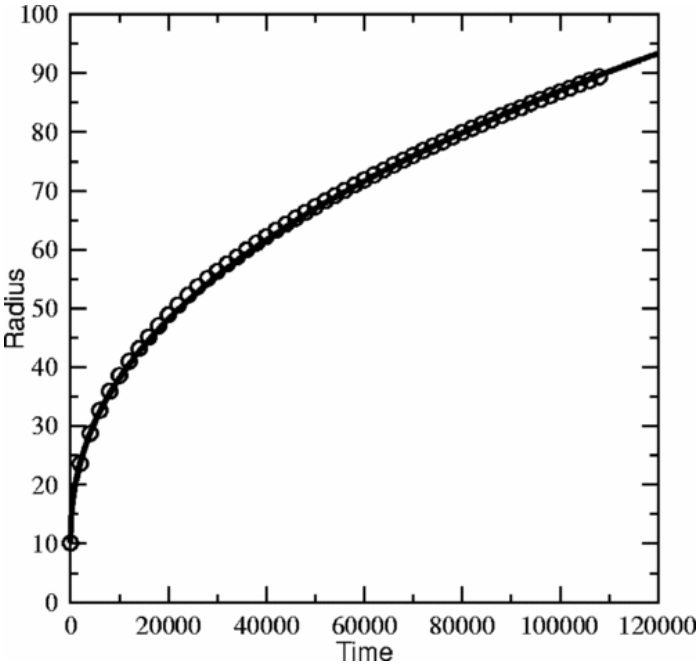

Figure 3.2: Radial penetration of liquid vs. time taken from Hyväluoma *et al.* (2006)

3.3 Capillary Penetration in Paper and Evaporation

As mentioned above, the underlying mathematical model to describe capillary flow in porous media is the Lucas-Washburn model. However, the validity of this model is still being analyzed. Meanwhile, the development of sophisticated models for capillary penetration allows us to model complex multi-phase flow in porous media. Hyväluoma *et al.* (2006) have estimated multi-phase liquid penetration in a paper using the Lattice-Boltzmann (LB) method. LB method, with spatially updating rules, makes it possible to handle fluid-solid boundaries. A set of two-dimensional radial penetration simulations were performed, and the penetration distance (radius) vs. time is shown in 3.2. The plot shows that the time taken to travel a particular length is non-linear. This result can be used as a reference to validate the simulation and experimental results obtained from this study and understand the effects of geometry on time taken to travel a known length.

An important factor affecting capillary flow is evaporation, especially for highly volatile liquids such as reacting reagents in lateral flow assays. Although Lucas-Washburn is a good approximation for one-dimensional penetration, a two-dimensional simulation requires a model based on Darcys law. Liu *et al.* (2018) formulated a theoretical model that considers the effects of evaporation along with geometry on capillary penetration in porous media. In addition to this, they performed two-dimensional and three-dimensional finite element analysis using COMSOL and estimated the effects of geometry on fluid flow rate.

Figure 3.3 represents the geometry of the sample in interest. The assumed geometry is a trapezoid with length(l_0), width of source edge (W_0), and width of sink edge (W_1). The dimension (l) represent the distance between the source edge and the liquid front at time t. Keeping l_0 constant, $\alpha = \frac{W_1}{W_0}$ determines the base angle of the trapezoid.

Figure 3.4 shows the impact of geometry, represented by α, on fluid penetration as a function of time. The distance on the vertical axis and the time on the horizontal axis are normalized by using the length of the trapezoid (l_0) and the time taken to travel l_0 for a sample geometry with $\alpha = 1$, represented by t_0. Liu *et al.* (2018) concluded that as the base angle increases the fluid front velocity is significantly reduced and vice versa.

The above-mentioned theoretical model will be employed in this thesis to estimate the effects in Whatman filter paper using water as the fluid. The current study will complement the theoretical model by incorporating the effects of relative humidity and by validating the model by experimentation. The numerical plot will be used as a reference to validate the simulation and experimental results obtained in this thesis.

While capillary penetration is modeled using the above-mentioned theoretical model, the simulation for evaporation and transport of water vapor requires a more

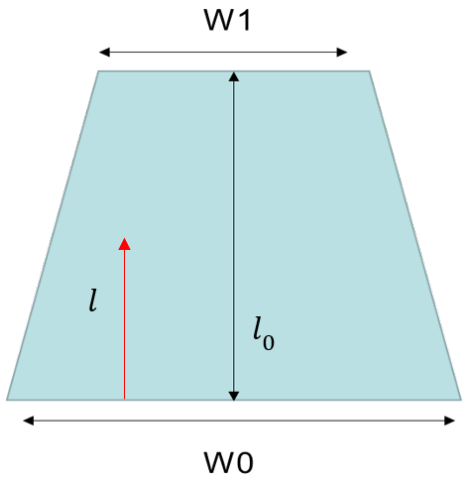

Figure 3.3: A schematic representing the geometry of the sample

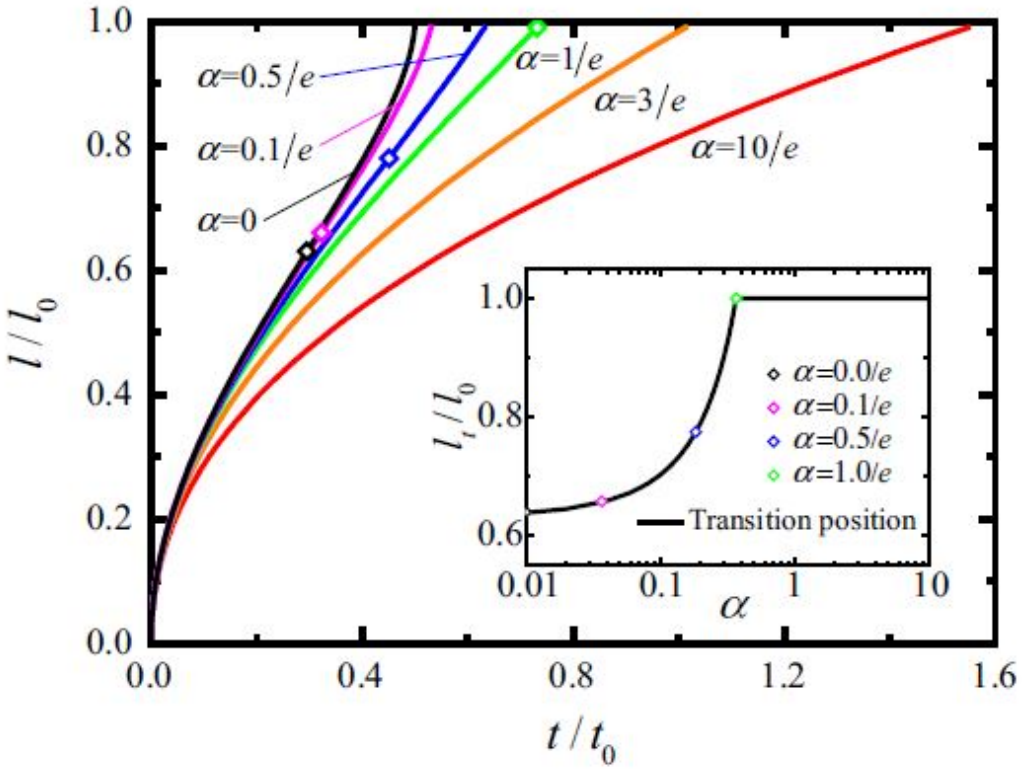

Figure 3.4: A plot showing the impact of geometry on capillary penetration in porous media. Figure was replicated from Liu *et al.* (2018)

fundamental formulation. Datta (2007a) and Datta (2007b) describe a detailed formulation of multiphase transport in porous media, including evaporation. The theoretical model utilizes Darcys law for transport in porous media, molecular diffusion for the transport of gases in porous media, and conservation of mass equations for phase change. This formulation will be employed to model evaporation in porous media.

Chapter 4

MODELLING OF FLUID FLOW IN POROUS MEDIA

This section describes the methodology for modeling porous media, fluids, mass and energy transport in porous media.

4.1 Non-Newtonian Fluid - Carreau Yasuda Model

As we discussed in 3.1, Non-Newtonian blood is defined by Carreau Yasuda model and the relation between dynamic viscosity and shear rate is give by equation 4.1.

$$\mu(\gamma) = \mu_\infty + (\mu_0 - \mu_\infty).[1 + (\lambda\gamma)^a]^{\frac{n-1}{2}} \tag{4.1}$$

where a, n, and λ are empirically determined constant parameters. The parameters a and n are dimensionless. The parameter λ is the relaxation time and has units of (s). μ_0 is the zero-shear viscosity, defined as the viscosity at zero shear rate. μ_∞ is the infinite-shear viscosity, defined as the viscosity at infinite shear rate and γ is the shear rate.

The main advantage of this model over other Non-Newtonian models is that it is continuous for all $\gamma \geq 0$. For blood with $n = 0.342$, the Carreau Yasuda model suggests that the dynamic viscosity is close to μ_∞ at high shear rates and therefore can be modeled as a Newtonian fluid with dynamic viscosity μ_∞. Similarly, at low shear rates, blood can be modeled as a Newtonian fluid with dynamic viscosity μ_0 (Boyd *et al.* (2007)). The parameters mentioned in table 3.1 determines the fluid behavior in Non-Newtonian regime between the two limiting cases μ_0 and μ_∞.

4.2 Lucas-Washburn Model

The Lucas-Washburn model assumes that any porous media is a bundle of parallel capillary tubes with one pore size (r) as shown in figure 3.1(A), and the equation to estimate the position of the liquid front is given by equation 4.2.

$$L^2(t) = \frac{\sigma.Cos(\theta).r}{2\mu}t \tag{4.2}$$

where $L(t)$ is the position of the liquid front as a function of time t. The relationship is determined by liquid surface tension (σ), contact angle (θ), and dynamic viscosity (μ) of the fluid. Further, $L(t)$ can be estimated experimentally and the contact angle of a liquid (θ) in any porous media can be determined by equating equation 4.2 to experimentally determined $L(t)$.

$$P_{capillay} = \frac{2.\sigma.Cos(\theta)}{r} \tag{4.3}$$

The capillary pressure inside the capillary tubes with a pore size (r) can be determined by equation 4.3 and will be used as an input parameter for simulating capillary flow in porous media.

4.3 Heat and Mass Transfer in Porous Media

Fluid transport in porous media can be due to three primary mechanisms molecular diffusion for gases, pressure-driven flow for gases, and capillary flow for liquids (Nield *et al.* (2006)). All these mechanisms are dependent on the fluid properties as well as the internal geometry of the solid matrix. Although a simple laminar flow through a complex pore structure can be assumed, simulating the fluid flow in porous media on a macro-scale can be computationally expensive. Therefore, a continuum approach is more desirable, and the following transport mechanisms incorporate ma-

terial properties to estimate the fluid behavior on a scale that is close to Lateral Flow Immunoassays.

Molecular diffusion of gases, such as water vapor and air, is described by Ficks law as shown in equation 4.4.

$$n_g^{diff} = -D_g.\frac{\partial C_g}{\partial S} \tag{4.4}$$

where n_g^{diff} is the mass flux due to diffusion, C_g is the gas concentration, S is the distance and D_g is the molecular diffusivity of the gas in porous media. The molecular diffusivity of gas in porous media is related to the gas diffusivity in bulk (D), porosity (ϕ) and tortuosity (τ_p) as shown in equation 4.5.

$$D_g = -D.\frac{\phi}{\tau_p} \tag{4.5}$$

Transport of gases in porous media due to pressure gradient is defined by Darcy's law as shown in equation 4.6

$$n_g^{press} = -\frac{\rho_g.K_g}{\mu_g}.\frac{\partial P}{\partial S} \tag{4.6}$$

where n_g^{press} is the mass flux due to pressure gradient, P is the total gas pressure, S is the distance, ρ_g and μ_g are the density and dynamic viscosity of the gas respectively. The permeability of the gas phase k_g is given by $K.K_{gr}$, where K is the intrinsic permeability of the porous media and K_{gr} is the relative permeability of the gas.

Similarly, Darcys law can be applied to liquid flow in porous media due to gas pressure on liquid and capillary pressure. The capillary attraction between liquid molecules and the walls of the porous media results in negative pressure (P_{cap} or P_c) given by equation 4.3. Therefore, the mass flux of liquid due to a pressure gradient can be written as equation 4.7.

$$n_l^{press,cap} = -\frac{\rho_l.K_l}{\mu_l}.\frac{\partial(P - P_c)}{\partial S} = -\frac{\rho_l.K_l}{\mu_l}.\frac{\partial P}{\partial S} + \frac{\rho_l.K_l}{\mu_l}.\frac{\partial P_c}{\partial S} \tag{4.7}$$

where $n_l^{press,cap}$ is the mass flux of liquid due to the pressure gradient. K_l is the permeability of liquid phase and is given by $K.K_{lr}$, where K is the intrinsic permeability of the porous media and K_{lr} is the relative permeability of the liquid.

The capillary pressure is a function of concentration and temperature, and, in the case of water, the relationship is given by moisture characteristic curves that are specific to involved materials. Since P_c is a function of temperature (T) and concentration (C), equation 4.7 can be re-written as equations 4.8 and 4.9.

$$n_l^{press,cap} = -\frac{\rho_l.K_l}{\mu_l}.\frac{\partial P}{\partial S} + \frac{\rho_l.K_l}{\mu_l}.\frac{\partial P_c}{\partial C}.\frac{\partial C}{\partial S} + \frac{\rho_l.K_l}{\mu_l}.\frac{\partial P_c}{\partial T}.\frac{\partial T}{\partial S} \tag{4.8}$$

$$n_l^{press,cap} = -\frac{\rho_l.K_l}{\mu_l}.\frac{\partial P}{\partial S} - D_C.\frac{\partial C}{\partial S} - D_T.\frac{\partial T}{\partial S} \tag{4.9}$$

where $D_C = -\frac{\rho_l.K_l}{\mu_l}.\frac{\partial P_c}{\partial C}$ and $D_T = -\frac{\rho_l.K_l}{\mu_l}.\frac{\partial P_c}{\partial T}$ are the capillary diffusivities due to concentration gradient and temperature gradient, respectively. Although the capillarity is modeled as diffusion terms, the actual mechanism is pressure driven.

If the porous media is entirely saturated, the capillary diffusivity due concentration gradient is negligible. Similarly, if the porous media is highly unsaturated, the capillary diffusivity due to concentration gradient dominates the capillary diffusivity due to the temperature gradient.

Evaporation can be included by including conservation equation while solving for the solution. After re-arranging the above equations, the transport of water liquid, water vapor, and air are given by equations 4.10, 4.11, and 4.12.

$$n_a = -\rho_a.\frac{K_g}{\mu_g}.\nabla P - \frac{C_g^2}{\rho_g}.M_a.M_v.D_{eff.g}.\nabla\frac{P - P_V}{P} \tag{4.10}$$

$$n_v = -\rho_v.\frac{K_g}{\mu_g}.\nabla P - \frac{C_g^2}{\rho_g}.M_a.M_v.D_{eff.g}.\nabla\frac{P_V}{P} \tag{4.11}$$

$$n_w = -\rho_w.\frac{K_w}{\mu_w}.\nabla P - D_w.\rho_w.\phi\nabla S_w - D_T.\nabla T \tag{4.12}$$

where n_a, n_v and n_w are the mass flux of air, vapor, and liquid water respectively. D_w and S_w are the diffusivity and saturation of liquid water in porous media, respectively. Evaporation rate results in phase change, and that is included by using the conservation of mass equation.

$$\frac{\partial C_v}{\partial t} + \nabla n_v = I' \tag{4.13}$$

$$\frac{\partial C_w}{\partial t} + \nabla n_w = -I' \tag{4.14}$$

$$\frac{\partial C_a}{\partial t} + \nabla n_a = 0 \tag{4.15}$$

Equations 4.13, 4.14, and 4.15 define the phase change of liquid water into water vapor and the evaporation rate is given by I'. Since evaporation results in mass loss from the liquid phase, the mass transport side of the equation (left-hand side) is equated to $-I'$. Since air does not participate in phase change, the mass transport of air is equated to 0.

The numerical analysis solves for seven variable ($n_v, n_w, n_a, C_v, C_w, C_a$, and I'). Therefore, an additional equation is required besides the six mass transport equations (4.10, 4.11, 4.12, 4.13, 4.14, and 4.15). Conservation of heat energy provides us with enough equations to solve for seven variables and is given by equation 4.16

$$(\rho C_p)_{eff}.\frac{\partial T}{\partial t} + \underbrace{\nabla(n_v.h_v + n_a.h_a + n_w.h_w)}_{convection} = \underbrace{\nabla(K_{eff}.\nabla T)}_{conduction} - \underbrace{\lambda I'}_{evaporation} + \underbrace{q'}_{heat} \quad (4.16)$$

where I' is the volumetric evaporation rate that can vary with time, h_v, h_a, h_w are the enthalpies of vapor, air, and water, respectively. The effective properties ρC_p and K_{eff} are given by equation 4.17 and 4.18.

$$(\rho C_p)_{eff} = \rho_s C_{ps}(1-\phi) + \rho_w C_{pw}\phi S_w + \rho_g C_{pg}\phi(1-S_w) \quad (4.17)$$

$$K_{eff} = K_s(1-\phi) + K_w\phi S_w + K_g\phi(1-S_w) \quad (4.18)$$

where C_{ps}, C_{pw}, and C_{pg} are specific heats of solid, water and gas phase, respectively. The above mentioned equations will be solved using finite element analysis to simulate evaporation in porous media.

4.4 Fluid Flow Rate and Geometry

To estimate the effects of geometry and evaporation, a two-dimensional porous media is assumed with dimensions, as shown in figure 3.4. It is assumed that the evaporation takes place from both the front and back sides of the sample, and the evaporation is negligible from edges of the sample. The evaporation in porous media can be modeled as viscous pressure loss at the fluid front and is given by equation 4.19.

$$P_{loss} = \mu.\frac{me'}{K.\rho.H}.\left[\left(l + \frac{l_0}{\alpha - 1}\right)^2.ln\left(1 + \frac{l}{l_0}.(\alpha - 1)\right) - \frac{l}{2}.\left(l + \frac{2.l_0}{\alpha - 1}\right)\right] \quad (4.19)$$

where H is the thickness of the sample, μ is the dynamic viscosity, m'_e is the evaporation rate, and K is the permeability. This viscous pressure loss results in effective

capillary pressure given by equation 4.20.

$$P_{eff} = P_{cap} - P_{loss} \tag{4.20}$$

where P_{cap} is calculated using equation 4.3. The effective capillary pressure is used as an input to Darcys model, and the Darcy velocity at the fluid front (l) is determined. Since the effective capillary pressure is to be applied at the moving fluid front; the simulation employs a moving mesh interface to iteratively apply the effective capillary pressure as a function of l.

Chapter 5

FIELD EXPERIMENT METHODOLOGY

The objective of this section is to discuss an experimental methodology that can validate the finite element analysis results and determine a mathematical model that can estimate the fluid flow rate for a given relative humidity, temperature, geometry, and grade of material.

A design of experiments technique was employed to study the effects of controllable factors (relative humidity, temperature, geometry, and grade of material) on a response variable (time taken to travel a specified distance). A full factorial experimental design was used to estimate the effects of individual factors as well as the interaction of factors on the response variable. A full factorial experimental design enables us to screen the significant factors affecting the response variable, optimize the factor settings that result in desirable response values, build a mathematical model that represents the process and verify the system behavior with the existing theory.

5.1 Experimental Design

The full factorial experiment is the experimental strategy used to vary factors together, instead of one at a time. Based on the number of levels of each of the factors, a full factorial experiment with $2^3.3^2$ design was employed. The description of each factor and its levels are described below, and the levels of these factors are shown in table 5.1. Factors such as wind velocity, fluid viscosity, and fluid temperature are excluded from the study and can be attributed to the intercept in the experimentally derived mathematical model.

Table 5.1: Factors and levels for design of experiments

Factors	Low level	Medium level	High level
Grade of material	Grade 1	-	Grade 42
Temperature	12 ^0C	23 ^0C	31 ^0C
Relative humidity	27 %	-	43 %
α	0.33	1	3

- Grade of material: Grade of Whatman filter paper takes into consideration of pore size, porosity, and other material-specific parameters. Therefore, effects due to all these parameters are lumped to simplify the model. The grade of the material was assigned as categorical (discrete) quantity with two levels. For this study, the term material and grade of material are interchangeable, although they are made up of nitrocellulose.

- Temperature: The experimental ambient temperature is maintained at a constant level through each of the experiments. The temperature variable was assigned as a continuous variable with three levels

- Relative humidity: A constant experimental humidity was maintained throughout the experiment trial. The humidity variable was assigned as a continuous variable with two levels

- α: Multiple ratios of the fluid sink width (W_1) to the fluid source width (W_0) of the paper specimen were assumed throughout the experimental trial. The variable was assigned as a continuous variable with three levels. For simplicity, α is also denoted as alpha.

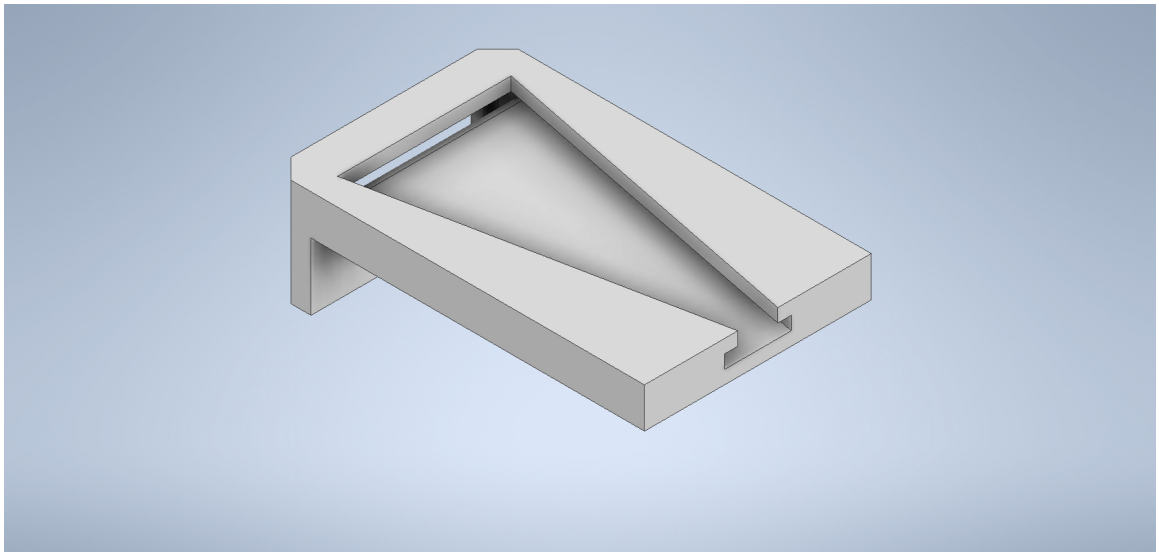

Figure 5.1: CAD model of a cassette with $\alpha = 0.33$

5.2 Experimental Setup

To facilitate the design of experiments, a set of six cassettes with different geometry were 3D printed to hold the nitrocellulose in place and in contact with the water source. The CAD model of the cassette is shown in figure 5.1. A fluid source is 3D printed to hold six cassettes and to make sure the nitrocellulose in all the cassettes meet fluid at the same time. The CAD model of water source is shown in figure 5.2.

The intermediate α values were also tested to verify the trend of its influence on the fluid flow rate. A set of twenty experiments, three to five runs per experiment, were performed at varying ambient and material conditions, as discussed in table 5.1. The final setup with nitrocellulose towards the end of the trial is shown in figure 5.3. The white and blue interface indicates the fluid front. The obtained data is used to develop a statistical model and to validate the existing literature.

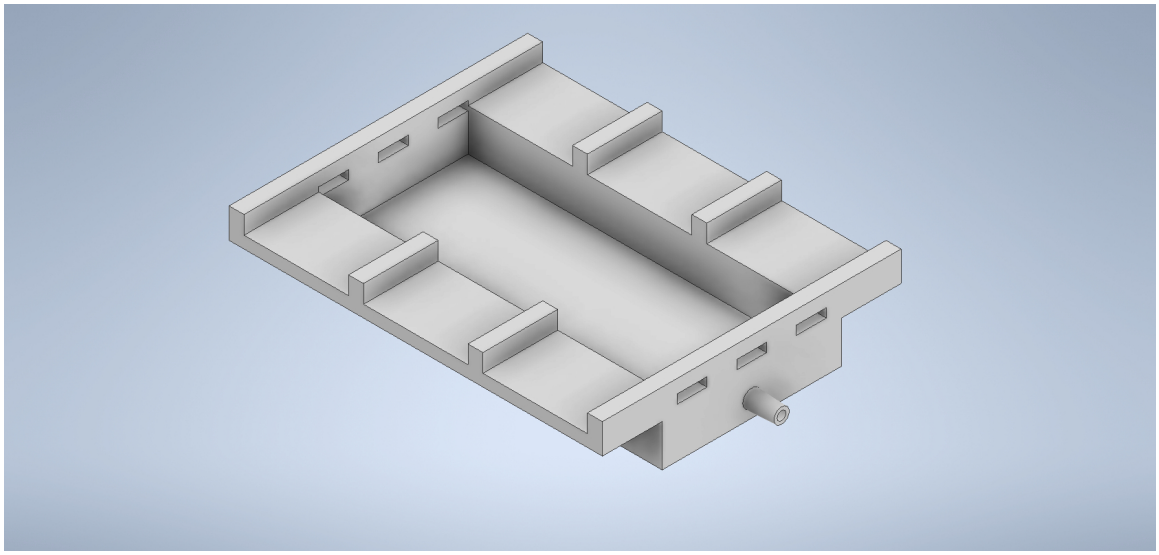

Figure 5.2: CAD model of the fluid source to hold six cassettes

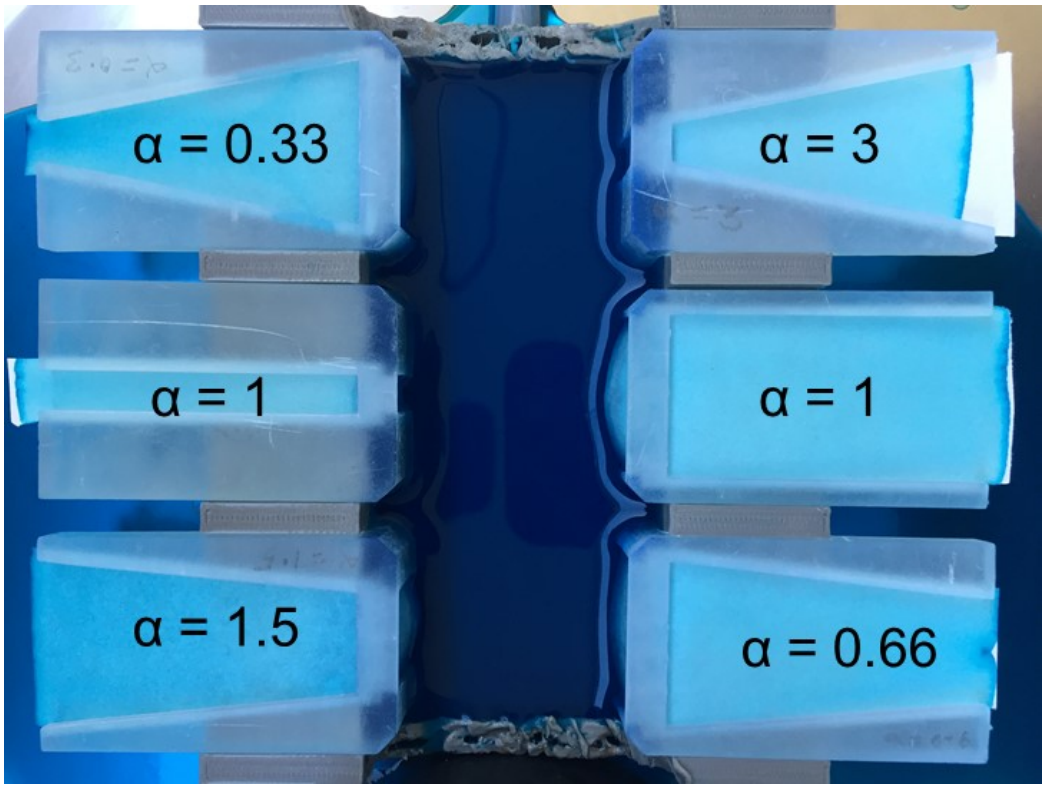

Figure 5.3: Photograph of the experimental setup for the design of experiments testing

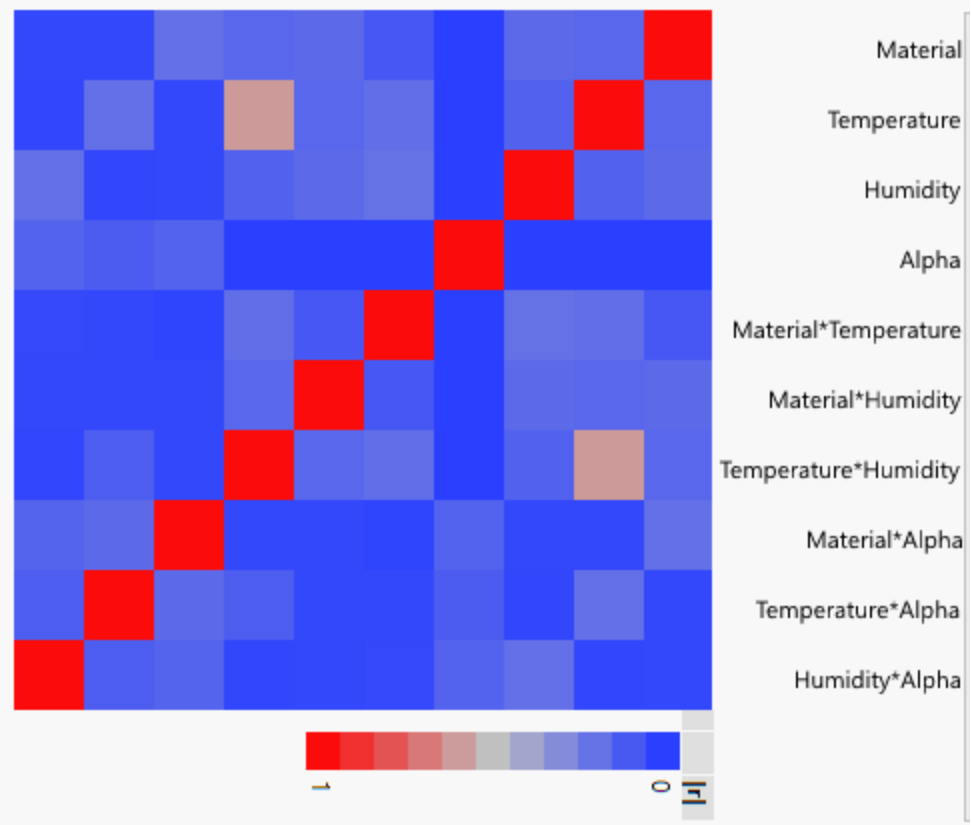

Figure 5.4: Correlation plot validating the design of experiments

5.3 Statistical Model Building and Design Evaluation

Design of experiments is a very powerful statistical that employs Standard Least Square Estimates method to fit the model with the considered factors against the response variable. This method was preferred over other ways as it finds the best fit for the given data by minimizing the sum of the errors of points from the plotted curve. Standard least squares approach is expected to offer low variance and low error for the given data.

The significant factors present in the design of experiments are expected to be the grade of material, temperature, relative humidity, and geometry. In addition to this,

the interaction of factors such as material and temperature, material and humidity, etc. also affect the response variable. The statistical estimates' validity can be verified by observing the correlation graph shown in figure 5.4. For the design of experiments to be valid, the factors should demonstrate zero correlation. From the correlation plot shown in figure 5.4, the negligible correlation between the factors can validate the experimental model.

Chapter 6

RESULTS

A set of finite element analyses were performed to simulate the effects of evaporation and geometry on fluid flow rate in porous media, and design of experiments was employed to conduct experimental studies. This section discusses the key findings from both the analyses and compares the obtained results with existing literature.

6.1 Finite Element Analysis

To estimate the effects of ambient conditions and geometry on the fluid flow rate in porous media, a set of finite element analyses were performed. First, as an effort to understand porous media modeling techniques, four different geometries and two different viscosity models were included. A pore-scale model, a simplified pore-scale model, the Lucas-Washburn model, and continuum model were compared using both Newtonian and Non-Newtonian fluids.

Later, evaporation in porous media is modeled by assuming the evaporation rate as a function of relative humidity. The concentration of water vapor in dry air is plotted to demonstrate evaporation from the wicking pad. Lastly, the combined effect of evaporation rate and geometry is modeled, and the trend concerning geometry is observed.

6.1.1 Porous Media Modelling

To investigate the effects of porous media modeling techniques, four different models are used with similar pore size and porosity. The different geometries are

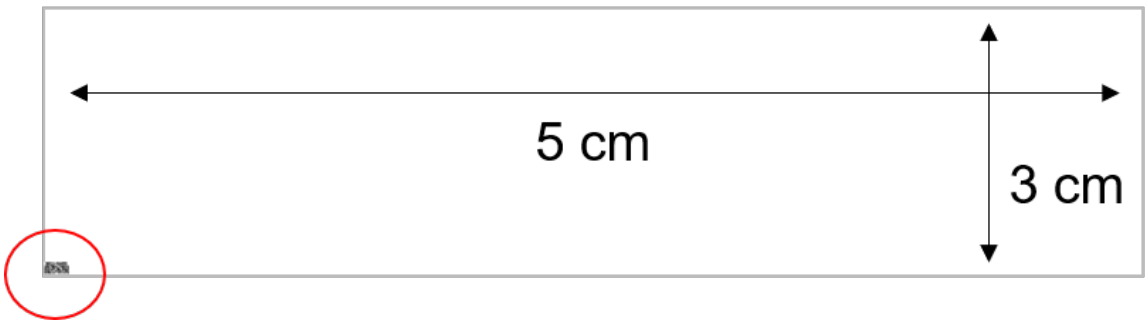

Figure 6.1: A schematic representation of the scale of application and the complexity of pore scale model

shown in figure 6.2. The colored surface indicates the interconnected pores, and the transparent structures represent the walls of the nitrocellulose membrane. All the samples are assumed to be $640\mu m\ X\ 320\mu m$.

A capillary pressure of $711Pa$ is applied at the source, and the estimated porosity is around 0.55 for all the models. Models (a), (b) and (c) represent the micro-scale structures of a porous media, and therefore, properties like pore-size, porosity and tortuosity affect the fluid flow rate and, in case of Non-Newtonian fluids, dynamic viscosity as well. The velocity profiles of Non-Newtonian fluid is shown in 6.3(a), (b), and (c). The dynamic viscosity of a Newtonian fluid is constant, therefore, the viscosity profiles of Non-Newtonian fluids are shown in 6.4 (a), (b), and (c).

Figure 6.1 demonstrates the scale of the pore scale model and the LFIA sample. The emphasized section of the image represents the pore-scale model. Simulating such a complex pore structure for macro-scale is impractical and computationally expensive. Therefore, model (d) shown, assumes the porous media as a simple rectangle and utilizes a continuum approach to estimate fluid behavior. The velocity profiles and dynamic viscosity profiles are shown in 6.3(d) and 6.4(d), respectively.

From plots 6.3 and 6.4 we can observe that the fluid behavior is dependent on pore structure. Since blood is is shear-thinning fluid, the dynamic viscosity reduces

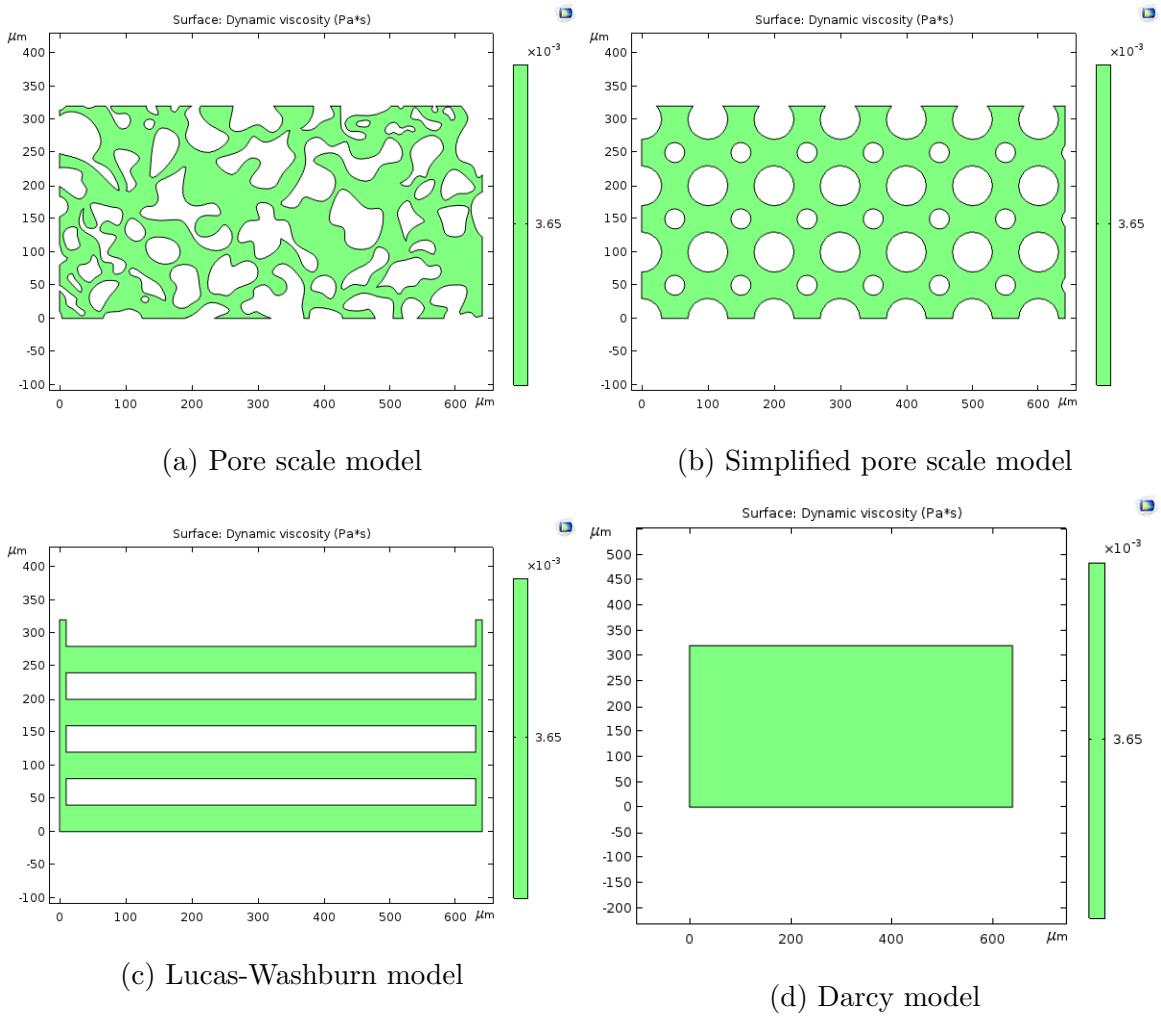

(a) Pore scale model

(b) Simplified pore scale model

(c) Lucas-Washburn model

(d) Darcy model

Figure 6.2: A set of two dimensional models representing a porous media

significantly at locations with high velocities and vice versa. Similarly, all the mentioned 2D models are simulated using blood modeled as a Newtonian fluid, and the fluid flow rates are compared.

Table 6.1 compares the difference in various porous media models as well as fluid models. When comparing the porous media model, the fluid velocities for both Newtonian and Non-Newtonian fluids are in the same order of magnitude and, Darcy model estimation is within the range of estimated velocity values. However, when comparing fluid models in any porous media model, the fluid velocities are overestimated in the

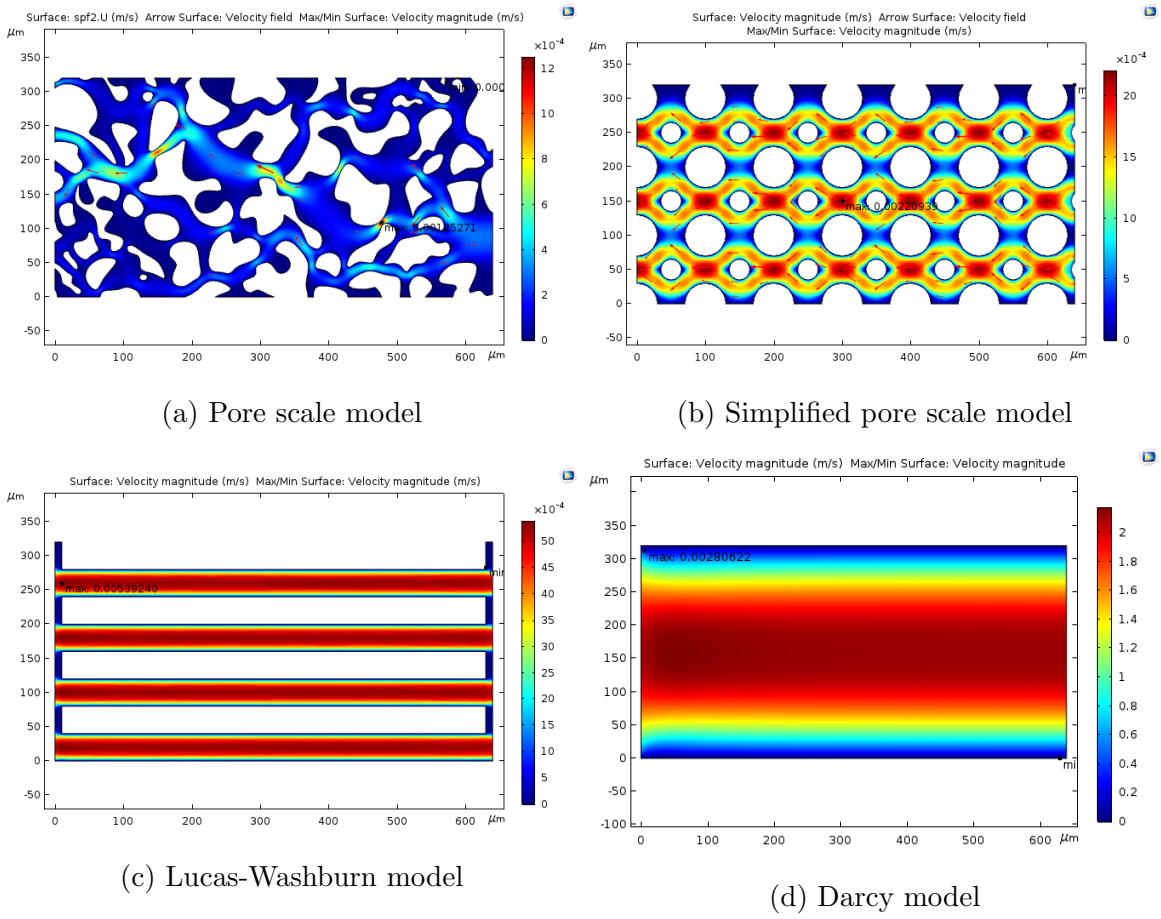

(a) Pore scale model

(b) Simplified pore scale model

(c) Lucas-Washburn model

(d) Darcy model

Figure 6.3: Velocity profiles of 2D models with Non-Newtonian fluid

Table 6.1: Comparison of porous media and fluid models

Porous media model	Newtonian fluid velocity	Non-Newtonian fluid velocity
Pore scale model	0.022 m/s	0.001 m/s
Simplified pore scale model	0.041 m/s	0.002 m/s
Lucas-Washburn model	0.062 m/s	0.005 m/s
Darcy model	0.053 m/s	0.001 m/s

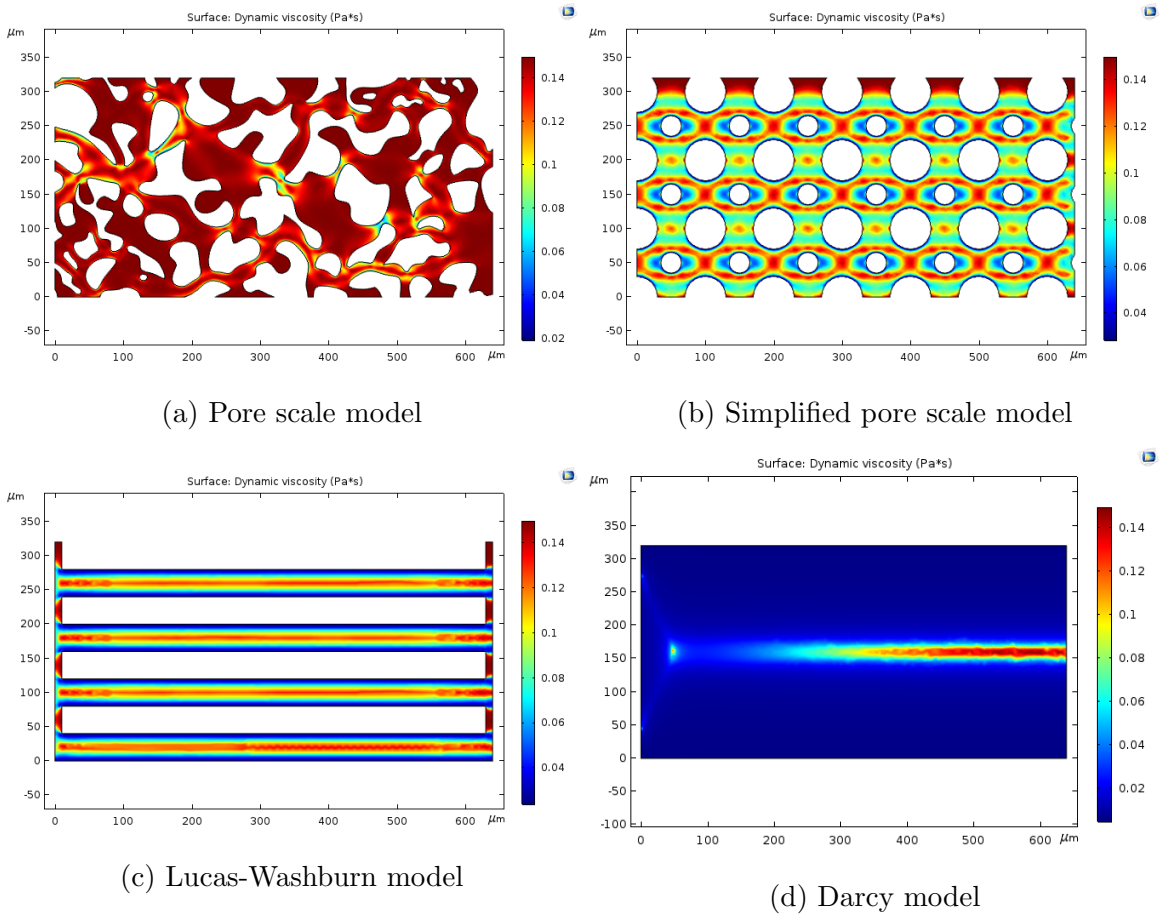

(a) Pore scale model

(b) Simplified pore scale model

(c) Lucas-Washburn model

(d) Darcy model

Figure 6.4: Dynamic viscosity profiles of 2D models with Non-Newtonian fluid

Table 6.2: Comparison of porous media model computation times

Porous media model	Computation time	Est. computation time for LFIA
Pore scale model	7 s	257 hrs
Simplified pore scale model	3 s	95 hrs
Lucas-Washburn model	3 s	118 hrs
Darcy model	3 s	3 s

Newtonian model. Therefore, it is crucial to model blood as Non-Newtonian fluid when the application results in intermediate fluid velocities. Newtonian model for blood is valid when the application results in either high or low fluid velocities.

Table 6.2 compares the computation time for each of the porous media models. Although the difference in computation times is not significant at micro-scale, the time taken to simulate a complex geometry at macro-scale can be extremely long. However, the computation time for the Darcy model at macro-scale is very short, mainly due to the continuum approach and the lack of complex geometry. Since the fluid flow rates estimated by Darcy model are within the range of estimated values and the time taken by Darcy model is short, this model is preferred for both Newtonian and Non-Newtonian fluids for macro-scale simulations. Therefore, all the subsequent finite element analyses will be based on the Darcy model.

6.1.2 Evaporation in Porous Media

To demonstrate evaporation in porous media, a two-domain system is modeled, as shown in figure 6.5. Dry air is included to track the concentration of water vapor in the air, and the flow is assumed to be unidirectional for demonstration purpose. The simulation utilizes the equations discussed in section 4.3. In addition to this, the evaporation rate as a function of relative humidity is included to understand the effects of relative humidity on evaporation in porous media. Therefore, a set of experimental analyses were performed to estimate the evaporation rate as a function of relative humidity.

The experiment and the subsequent simulations were carried out using Grade 1 Whatman filter paper with a pore size of 11 μm, the porosity of 0.55, and dimensionless permeability of 0.0063. The estimated evaporation rate function is given by equation 6.1 and the plot is shown in figure 6.6

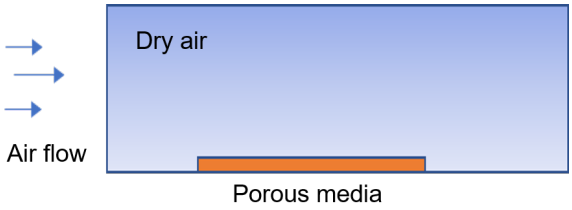

Figure 6.5: A schematic representation of FEM model to simulate evaporation in a porous media

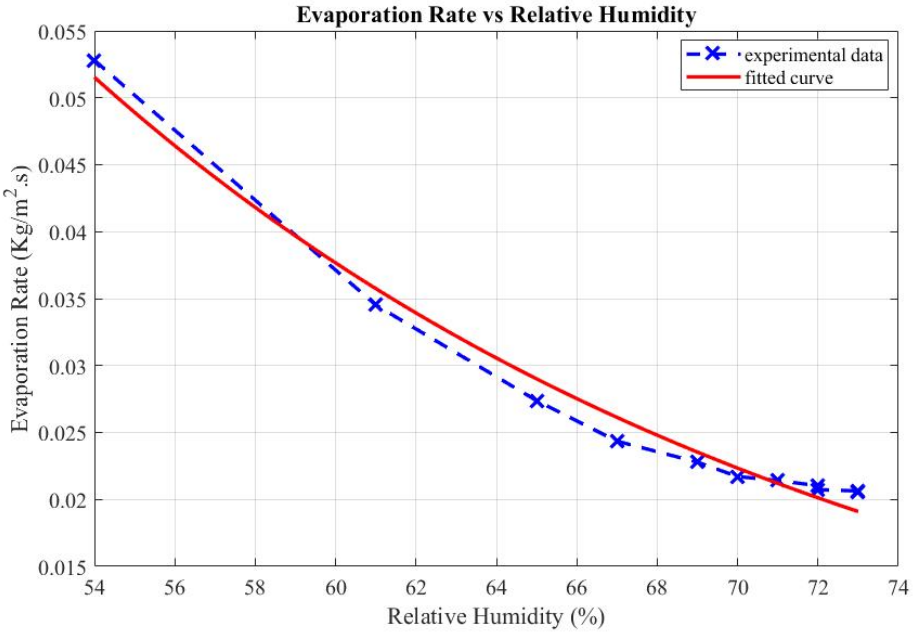

Figure 6.6: Experimental estimation of evaporation rate as a function of relative humidity

$$m'_e(RH) = 0.6913.\ e^{-0.049(RH)} \tag{6.1}$$

where m'_e is the evaporation rate and RH is the relative humidity.

Equation 6.1 is plugged into the simulation, and the water vapor concentration as a function of time at a given relative humidity is plotted. Figure 6.7 shows the difference in molar concentration of escaped water vapor at 1% and 97% relative

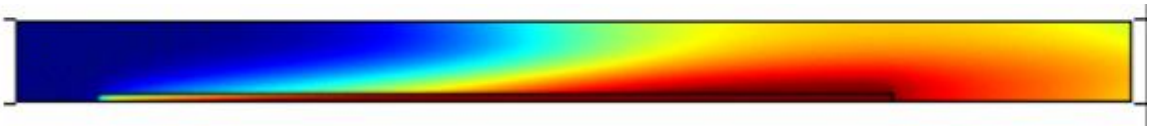

(a) Evaporation at 1% RH

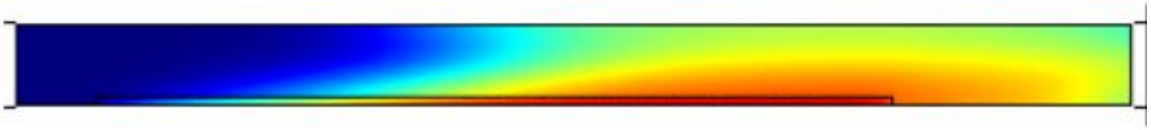

(b) Evaporation at 97% RH

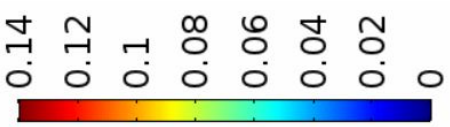

(c) Concentration color scale in mol/m^3

Figure 6.7: Water vapor concentration (mol/m^3) in dry air at 1% and 97% relative humidity

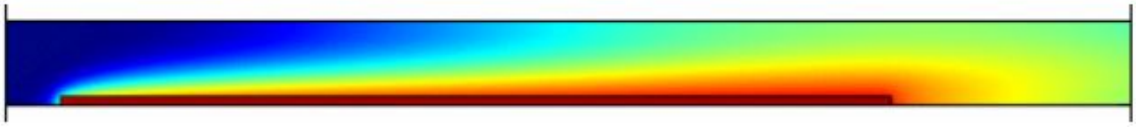

(a) High evaporation

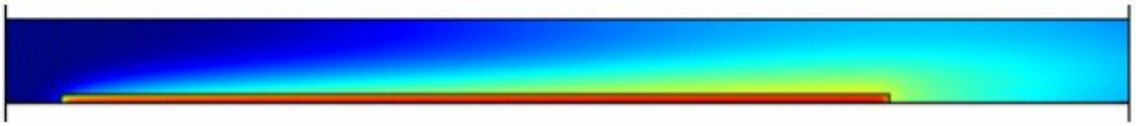

(b) Low evaporation

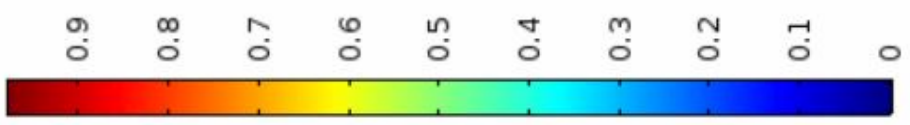

(c) Concentration color scale in mol/m^3

Figure 6.8: Evaporation in porous media with extreme evaporation rates

humidity. This analysis suggests that the evaporation in porous media is inhibited by high relative humidity. To demonstrate evaporation in porous media, figure 6.8 shows the molar concentration of water vapor in dry air at extremely high and low evaporation rates. These set of results can be used to understand evaporation of any analyte in LFIA, especially the reagents with high volatility.

6.1.3 Fluid Flow Rate in Porous Media

To estimate the influence of evaporation and geometry on fluid flow rate in porous media, a set of simulations with varying α were performed. The physics behind these simulations were discussed in section 3.3. The effective capillary pressure, given by equation 4.20, is applied as the pressure at the fluid front. Since the fluid front is moving, a moving mesh interface was employed.

A set of transient analyses were performed to estimate fluid velocity as a function of time. The geometry of the nitrocellulose sample was changed by varying α from 0.33 to 3. Figure 6.9 shows the sequence of estimated fluid flow rates from the transient analysis. It can be observed that the fluid flow rate in both $\alpha = 0.6$ and $\alpha = 1.5$ reduces as shown in figures 6.9 (a) $\rightarrow$ (c) $\rightarrow$ (d) as well as (b)$\rightarrow$ (d) $\rightarrow$ (e). However, in the sample with $\alpha = 0.6$, the maximum velocity towards the end of the analysis is at the sink side. Whereas, in the sample with $\alpha = 1.5$, the maximum velocity towards the end of the analysis is at the source edge.

The fluid velocities as a function of time for samples with $\alpha = 0.5$, and 1.5 are plotted as shown in figure 6.10. The horizontal axis represents time (t) and the vertical axis represents velocity. The simulated results closely align with the existing literature, as discussed in section 3.3.

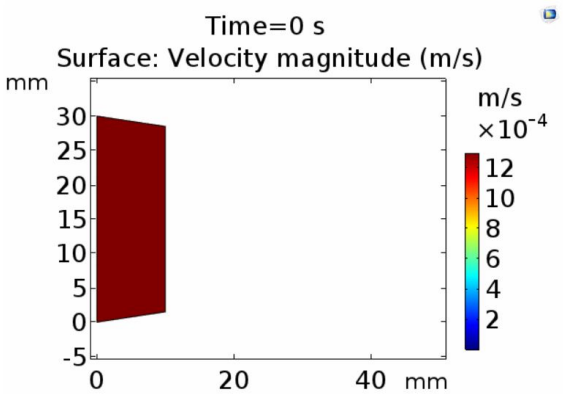

(a) Velocity at t_0 for $\alpha = 0.6$

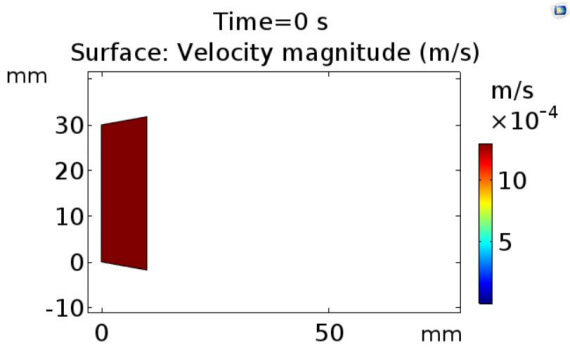

(b) Velocity at t_0 for $\alpha = 1.5$

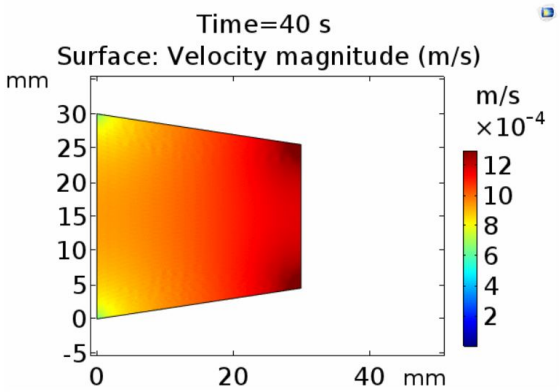

(c) Velocity at t_1 for $\alpha = 0.6$

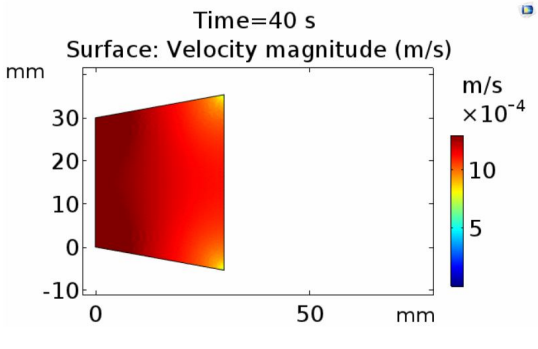

(d) Velocity at t_1 for $\alpha = 1.5$

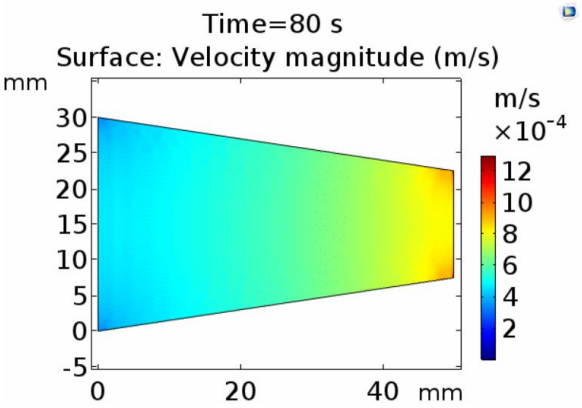

(e) Velocity at t_2 for $\alpha = 0.6$

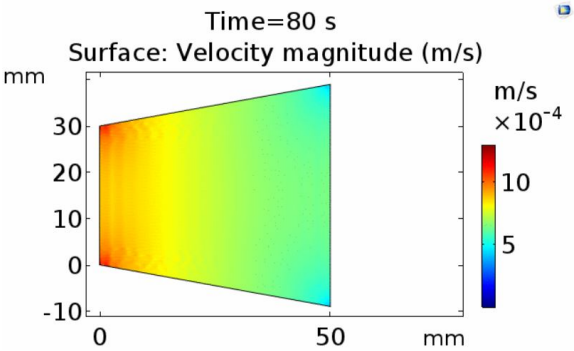

(f) Velocity at t_2 for $\alpha = 1.5$

Figure 6.9: Fluid velocity plots for $\alpha = 0.6$ and $\alpha = 1.5$ at different times

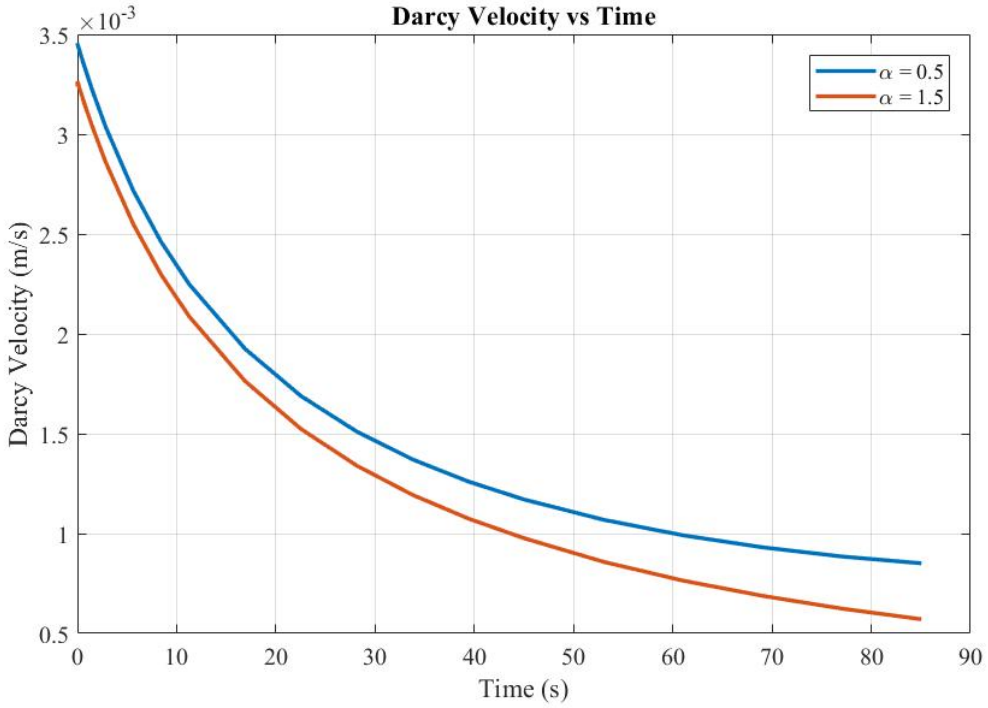

Figure 6.10: Effect of evaporation and geometry on the fluid flow rate in porous media

6.2 Experimental Analysis

To validate the simulation results as well as the findings from Liu *et al.* (2018), design of experiments statistical tool has been employed as discussed in chapter 5. This tool helps us to determine significant factors and estimate the parametric coefficients of the model using linear regression techniques. The estimated parametric coefficients are shown in table 6.3.

From the fitted model, the significant factors are found to be Intercept, Grade of material, Relative humidity, α, and Grade of material X α. Although the temperature is expected to be a significant factor affecting the evaporation rate, the estimates suggest that the influence of temperature on time taken to travel 5 cm is insignificant as compared to other factors. This anomaly can be attributed to the range of temperatures employed during the experiment. Since the temperature difference is around

Table 6.3: Estimation of parametric coefficients using linear regression techniques

Term	Estimate	Std Error	t ratio	Prob¿[t]
Intercept	16.0027	0.6421	24.9200	< 0.0001
Grade of material [M]	-4.5874	0.6875	-6.6700	< 0.0001
Temperature [T]	0.3469	1.1075	0.3100	0.7605
Relative humidity [RH]	-3.6537	0.6421	-5.6700	< 0.0002
α	4.4156	0.7142	6.1800	< 0.0001
Grade of Material X Temperature	0.0367	0.7785	0.0500	0.9638
Grade of Material X Relative humidity	1.1571	0.6771	1.7100	0.1183
Temperature X Relative humidity	0.4183	1.0988	0.3800	0.7114
Grade of material X α	-2.1855	0.7164	-3.0500	0.0122
Temperature X α	0.6340	0.8362	0.7600	0.4658
Relative humidity X α	-1.4951	0.7143	-2.0900	0.0628

19 ^0C, the effect due to temperature is not adequately represented in the analysis.

The parametric estimates can be used to determine a statistical model, and this is done by including the most significant factors as well as interactions. The mathematical model is derived, as shown below.

$$t_{5cm} = 23.43 + 7.13.\alpha - 4.59.M - 0.34.RH - 0.24.T -$$
$$0.14.\alpha.RH + 0.05.\alpha.T + 0.01.RH.T - 4.92.M.RH - 0.079.M.T + 1.09.M.\alpha$$

where t_{5cm} is the time taken to travel 5 cm.

For a given application and the fluid in interest, a similar statistical model can be determined. Such models are useful to find the optimal conditions for the desired

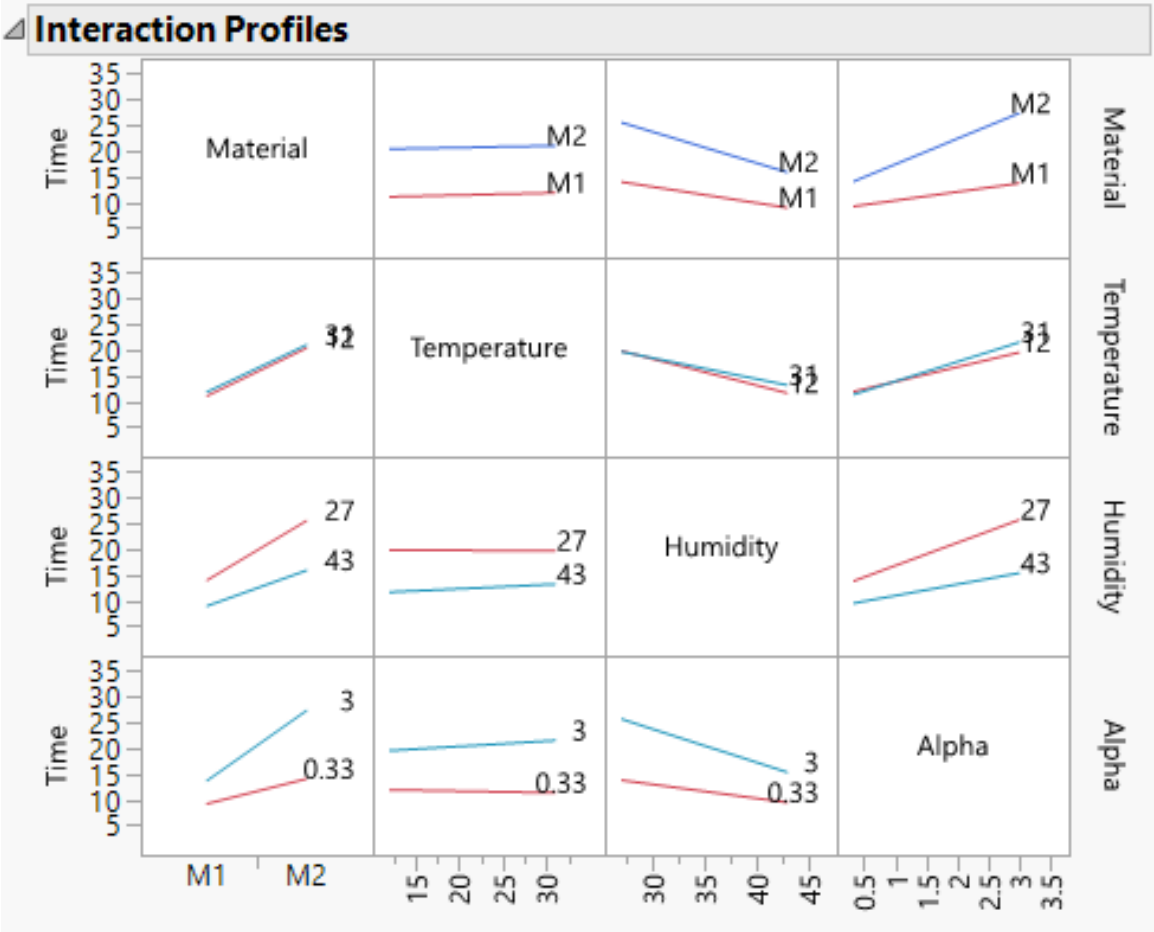

Figure 6.11: Interaction plot representing the relation between each of the factors and the response variable time or time taken to travel 5 cm (minutes)

response or to estimate the response as a function of included factors.

Design of experiments also produces full factorial interaction plots, as shown in figure 6.11.

The interaction plots are to be read as a two-dimensional matrix. For example, the plot corresponding to material and alpha (α) denotes the combined effect of the grade of material [M] and α on time taken to travel 5 cm. The plot suggests that varying the grade of material from grade 1 to grade 42 increases the time taken to travel a specified distance. In addition to this, the increase in α results in an increase

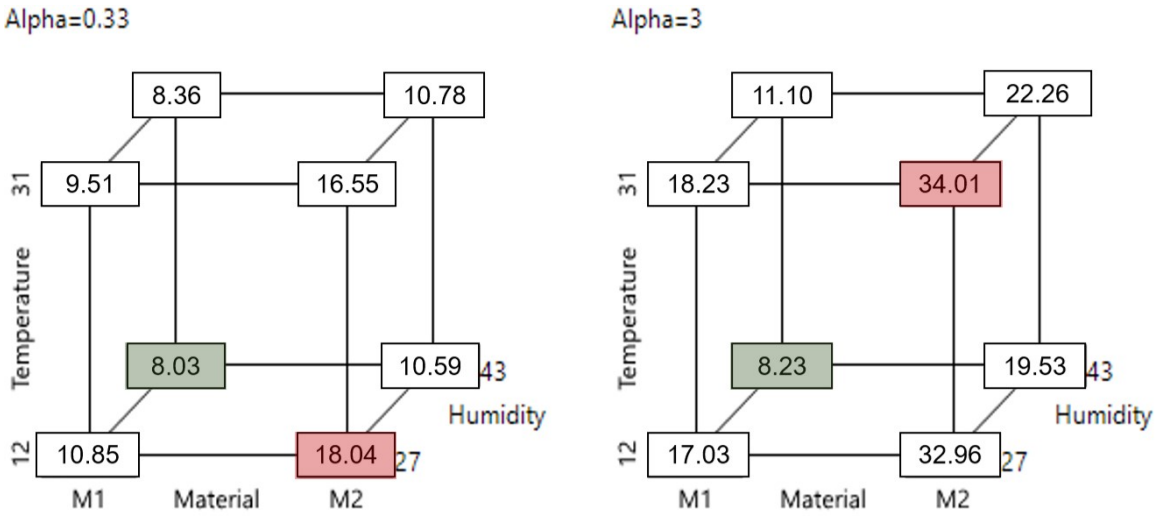

Figure 6.12: Cube plot representing the time of travel (min) as a function of the grade of material, temperature, and relative humidity for an alpha of 0.33 (left) and 3 (right). The conditions giving the fastest (green) and slowest (red) velocity are indicated for each cube plot

in time taken to travel a specified length for the same grade of material. These results closely align with the Whatman filter paper specification.

The cube plot, as shown in figure 6.12, generated by design of experiments, enables us to determine the optimal settings to achieve a desired time of travel. For example, to achieve a time of travel of 8.02 minutes, the ambient temperature should be maintained at 120C, the relative humidity at 43 %, with α= 0.33 in Whatman filter paper grade 1.

In addition to parametric estimates and cube plots, fluid front velocity as a function of time is determined using experimental analysis. The experimental results and simulation results are combined and plotted together by normalizing the velocities as well as time. Figure 6.13 shows the relation between the velocities and the geometry. The solid line corresponds to simulated results, and the broken line corresponds to experimental values.

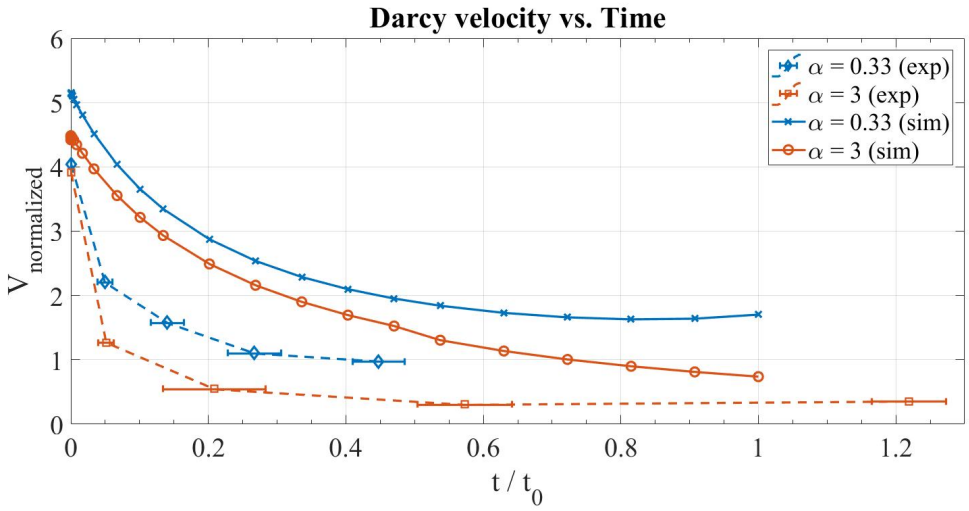

Figure 6.13: Simulated and experimental result showing the normalized velocity v.s. normalized time for fluid flow in varying geometries of porous media (cellulose) for Lateral Flow Immunoassays

For $\alpha = 0.33$ the experimental values stop at $t/t_0 = 0.5$. This suggests that the fluid front reached the 5cm mark twice as fast as the fluid front in a sample with $\alpha = 1$. Similarly, the fluid front in a sample with $\alpha = 3$ took almost 1.3 times longer than the fluid front in a sample with $\alpha = 1$ to reach the 5 cm mark. Hence, the values stop at $t/t_0 \simeq 1.3$.

The plot 6.13 also shows the difference between the simulated and the experimental values. This difference can be attributed to the pore size and capillary pressure. For simulation purposes, the capillary pressure is calculated using an average pore size of 11 μm, but in reality, the pore size in grade 1 Whatman filter paper varies from 2.5 μm to 19 μm. While calculating the capillary pressure using the equation 4.3, a contact angle of 1.309 *radians* is assumed for water (Cummins *et al.* (2017)).

Although Cummins *et al.* (2017) attempted to mitigate the inaccuracies in the Lucas-Washburn model while estimating the contact angle of water, the accuracy of the Lucas-Washburn model is still being studied. In addition to this, some of the

significant parameters that result in the variation are the uncontrolled factors such as wind velocity, fluid temperature, surface tension, etc.

However, Both finite element analyses and experimental analyses suggest that the velocity is decreasing with time and geometry of the sample determines the initial velocities and the rate at which the velocity is reduced. Therefore, the geometry of the sample can be tuned to achieve a desired fluid velocity.

Chapter 7

CONCLUSION AND FUTURE WORK

Lateral flow immunoassays offer many advantages as compared to other POC device and satisfy most of the assured criteria. However, the performance is limited by the non-ideal test conditions. The performance determining parameters like reagent stability and reaction rate are usually dependent on the fluid flow rate in porous media. Therefore, estimating the fluid flow rate in porous media for a given set of ambient conditions allows us to predict the efficiency and repeatability of the tests.

7.1 Conclusion

Literature suggests that temperature and relative humidity affect the evaporation rate and, evaporation rate results in viscous pressure loss. Therefore, the effective capillary pressure across the fluid source and the fluid front is altered. This study focuses on understanding the effects of relative humidity and temperature on fluid flow rate and the effect of geometry in tuning the fluid flow velocity. To achieve the objective, a set of numerical and experimental analysis were performed and are compared to existing literature.

To understand fluid flow in porous media, a set of finite element simulation was performed to compare various porous media modeling techniques. In addition to this, the effect of Newtonian and Non-Newtonian model of blood on fluid velocity is compared. Although pore-scale modeling closely represents the porous media, discretizing a complex geometry and solving partial differential equations can be computationally expensive. This study suggests that Darcy approximation or continuum approach of

porous media is more practical for macro-scale models such as lateral flow immunoassays and provide solutions within estimated values. However, a Newtonian approximation of a Non-Newtonian fluid such as blood requires close attention. The study suggests that Newtonian approximation overestimates the fluid velocity in porous media. Since blood is a shear-thinning fluid, a Newtonian approximation may be valid in cases where the fluid flow rate is relatively high or relatively low.

To estimate the evaporation in porous media, a set of experimental analyses were performed to determine the relationship between evaporation rates and relative humidity. The obtained relationship suggests that the relationship is exponential, and the evaporation rate decreases with increase in relative humidity. The obtained exponential function is plugged into the simulation to estimate the transport of water vapor in dry air. The evaporation in porous media as a function of relative humidity has been successfully simulated.

To estimate the combined effect of geometry and evaporation rate on fluid flow rate in porous media, a set of finite element analyses were performed. The study suggests that evaporation results in a viscous pressure loss and the fluid flow rate can be tuned using the base angle of the test strip. These findings were then validated using the design of engineering experiments. The design of engineering experiments included the combined effects of , temperature, relative humidity, and lumped porous media parameters on the fluid flow rate. The experimental study closely aligned with available mathematical models and obtained simulation results. A high fluid flow rate can be achieved at low temperature, high relative humidity, low , and a porous media that is close to grade 1 Whatman filter paper.

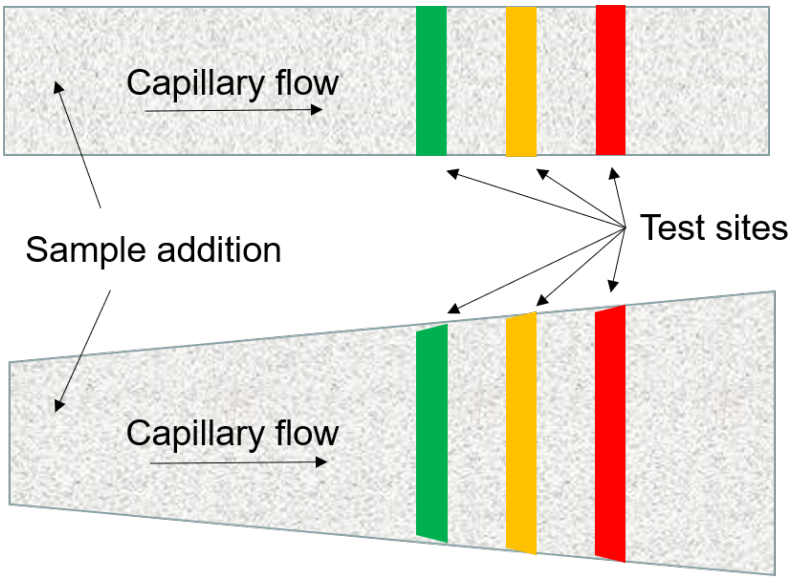

Figure 7.1: A schematic representing the application of this study

7.2 Future Scope

The current study derives the mathematical model using data obtained from experiments that were performed in ambient conditions. Although this test setup closely represents non-ideal test conditions, the uncontrollable nature of ambient temperature and humidity along with wind velocity results in significant intercept term in the mathematical model. Therefore, a refined mathematical model can be achieved by repeating the experiments in an environmental test chamber with controlled relative humidity and temperature.

In addition to this, the study focuses on determining the effects of geometry and evaporation on the flow rate of water. However, most of the lateral flow Immunoassays either use reagents with high volatility or Non-Newtonian analytes like blood. Therefore, the current study should be further refined using a specific fluid of interest to determine a mathematical model that closely represents the actual test.

Figure 7.1 is a schematic representation of a diagnostic test strip that is being

developed at Arizona State University. One of the challenges faced is the lack of an optimal fluid flow rate for reliable and repeatable antibody-receptor binding. The main requirement of the test is to limit the flow rate as the analyte travels from the green test site to the red test site. To address this, a nitrocellulose membrane with $\alpha > 1$ can be employed.

Bahadır, E. B. and M. K. Sezgintürk, "Lateral flow assays: Principles, designs and labels", TrAC Trends in Analytical Chemistry **82**, 286–306 (2016).

Boyd, J., J. M. Buick and S. Green, "Analysis of the casson and carreau-yasuda non-newtonian blood models in steady and oscillatory flows using the lattice boltzmann method", Physics of Fluids **19**, 9, 093103 (2007).

Chao, T. C., O. Arjmandi-Tash, D. B. Das and V. M. Starov, "Simultaneous spreading and imbibition of blood droplets over porous substrates in the case of partial wetting", Colloids and Surfaces A: Physicochemical and Engineering Aspects **505**, 9–17 (2016).

Chin, C. D., V. Linder and S. K. Sia, "Commercialization of microfluidic point-of-care diagnostic devices", Lab on a Chip **12**, 12, 2118–2134 (2012).

Cummins, B. M., R. Chinthapatla, F. S. Ligler and G. M. Walker, "Time-dependent model for fluid flow in porous materials with multiple pore sizes", Analytical chemistry **89**, 8, 4377–4381 (2017).

Datta, A., "Porous media approaches to studying simultaneous heat and mass transfer in food processes. i: Problem formulations", Journal of food engineering **80**, 1, 80–95 (2007a).

Datta, A., "Porous media approaches to studying simultaneous heat and mass transfer in food processes. ii: Property data and representative results", Journal of food engineering **80**, 1, 96–110 (2007b).

Fridley, G. E., C. A. Holstein, S. B. Oza and P. Yager, "The evolution of nitrocellulose as a material for bioassays", MRS bulletin **38**, 4, 326–330 (2013).

Gribble, C. M., G. P. Matthews, G. M. Laudone, A. Turner, C. J. Ridgway, J. Schoelkopf and P. A. Gane, "Porometry, porosimetry, image analysis and void network modelling in the study of the pore-level properties of filters", Chemical engineering science **66**, 16, 3701–3709 (2011).

Hyväluoma, J., P. Raiskinmäki, A. Jäsberg, A. Koponen, M. Kataja and J. Timonen, "Simulation of liquid penetration in paper", Physical Review E **73**, 3, 036705 (2006).

Kim, H., M. Prezzi and R. Salgado, "Calibration of whatman grade 42 filter paper for soil suction measurement", Canadian journal of soil science **97**, 2, 93–98 (2016).

Kumar, S., S. Kumar, M. A. Ali, P. Anand, V. V. Agrawal, R. John, S. Maji and B. D. Malhotra, "Microfluidic-integrated biosensors: Prospects for point-of-care diagnostics", Biotechnology journal **8**, 11, 1267–1279 (2013).

Lee, L., E. Nordman, M. Johnson and M. Oldham, "A low-cost, high-performance system for fluorescence lateral flow assays", Biosensors **3**, 4, 360–373 (2013).

Liu, M., J. Wu, Y. Gan, D. A. Hanaor and C. Chen, "Tuning capillary penetration in porous media: combining geometrical and evaporation effects", International Journal of Heat and Mass Transfer **123**, 239–250 (2018).

Mach, G., C. Sherif, U. Windberger, R. Plasenzotti and A. Gruber, "A non newtonian model for blood flow behind a flow diverting stent", in "Excerpt from the Proceedings of the 2016 COMSOL Conference", (2016).

Mathers, C. D. and D. Loncar, "Projections of global mortality and burden of disease from 2002 to 2030", PLoS medicine **3**, 11, e442 (2006).

Nield, D. A., A. Bejan *et al.*, *Convection in porous media*, vol. 3 (Springer, 2006).

Schito, M., T. F. Peter, S. Cavanaugh, A. S. Piatek, G. J. Young, H. Alexander, W. Coggin, G. J. Domingo, D. Ellenberger, E. Ermantraut *et al.*, "Opportunities and challenges for cost-efficient implementation of new point-of-care diagnostics for hiv and tuberculosis", Journal of Infectious Diseases **205**, suppl_2, S169–S180 (2012).

Sharma, S., J. Zapatero-Rodríguez, P. Estrela and R. O'Kennedy, "Point-of-care diagnostics in low resource settings: present status and future role of microfluidics", Biosensors **5**, 3, 577–601 (2015).

Yager, P., G. J. Domingo and J. Gerdes, "Point-of-care diagnostics for global health", Annual review of biomedical engineering **10** (2008).

BIOGRAPHICAL SKETCH

Nipun Thamatam graduated with his Bachelor's degree in Electrical Engineering from Birla Institute of Technology and Science (BITS), Pilani - Goa, India and is currently completing his Master's degree in Electrical Engineering at Arizona State University (ASU). Prior to joining ASU, he worked on his undergraduate thesis at Indian Space Research Organization and primarily focused on MEMS design and fabrication of inertial sensors for lunar applications. As a member of Bio-Electrical Systems and Technology Laboratory at ASU, he specializes in finite element analysis, and fluid mechanics in Biomedical applications. His thesis project focused on numerical modelling of fluid flow in porous media and experimental validation using statistical methods. He has industry experience in MEMS development and Sensor integration. After graduating, Nipun will be pursuing a doctoral degree in Electrical Engineering at Virginia Polytechnic Institute and State University (Virginia Tech).